Astronomy & Astrophysics manuscript no. ngc˙accepted˙language
May 23, 2016
© ESO 2016

Inferring the evolutionary stages of the internal structures of NGC 7538 S and IRS1 from chemistry

S. Feng[1,2], H. Beuther[1], D. Semenov[1], Th. Henning[1], H. Linz[1], E. A. C. Mills[3], R. Teague[1]

1. Max-Planck-Institut für Astronomie, Königstuhl 17, D-69117, Heidelberg
2. Max-Planck-Institut für Extraterrestrische Physik, Giessenbachstrasse 1, 85748, Garching, syfeng@mpe.mpg.de
3. National Radio Astronomy Observatory, 1003 Lopezville Road, Socorro, NM 87801, USA

May 23, 2016

arXiv:1605.03960v2 [astro-ph.GA] 20 May 2016

ABSTRACT

Context. Radiative feedback of young (proto)stars and gas dynamics including gravitational collapse and outflows are important in high-mass star-forming regions (HMSFRs), for the reason that they may leave footprints on the gas density and temperature distributions, the velocity profile, and the chemical abundances.
Aims. We unambiguously diagnose the detailed physical mechanisms and the evolutionary status of HMSFRs.
Methods. We performed 0.4″(∼ 1000 AU) resolution observations at 1.37 mm towards two HMSFRs, NGC 7538 S and IRS1, using the Plateau de Bure Interferometre (PdBI). The observations covered abundant molecular lines, including tracers of gas column density, hot molecular cores, shocks, and complex organic molecules. We present a joint analysis of the 1.37 mm continuum emission and the line intensity of 15 molecular species (including 22 isotopologues). Assuming local thermal equilibrium (LTE), we derived molecular column densities and molecular abundances for each internal gas substructure that is spatially resolved. These derived quantities are compared with a suite of 1-D gas-grain models.
Results. NGC 7538 S is resolved into at least three dense gas condensations. Despite the comparable continuum intensity of these condensations, their differing molecular line emission is suggestive of an overall chemical evolutionary trend from the northeast to the southwest. Line emission from MM1 is consistent with a chemically evolved hot molecular core (HMC), whereas MM3 remains a prestellar candidate that only exhibits emission of lower-excitation lines. The condensation MM2, located between MM1 and MM3, shows an intermediate chemical evolutionary status. Since these three condensations are embedded within the same parent gas core, their differing chemical properties are most likely due to the different warm-up histories, rather than the different dynamic timescales. Despite remaining spatially unresolved, in IRS1 we detect abundant complex organic molecules (e.g. NH_2CHO, CH_3OH, $HCOOCH_3$, CH_3OCH_3), indicating that IRS1 is the most chemically evolved HMC presented here. We observe a continuum that is dominated by absorption features with at least three strong emission lines, potentially from CH_3OH. The CH_3OH lines which are purely in emission have higher excitation than the ones being purely in absorption. Potential reasons for this difference are discussed.
Conclusions. This is the first comprehensive comparison of observations of the two high-mass cores NGC 7538 S and IRS1 and a chemical model. We have found that different chemical evolutionary stages can coexist in the same natal gas core. Our achievement illustrates the strength of chemical analysis for understanding HMSFRs.

Key words. Stars: formation; stars: early type; stars: individual: NGC 7538 IRS1; stars: individual: NGC 7538 S; ISM: lines and bands; ISM: molecules

1. Introduction

The ubiquitous multiplicity of high-mass star-forming regions (HMSFRs) leads to abundant dense gas cores and associated (proto-)stellar outflows, shocks, and disk-like structures. Understanding how dense gas structures and cores form and evolve in such clustered environments, and indeed how such massive stellar clusters come into the existence, requires high angular resolution millimetre and submillimetre interferometric observations.

However, the interpretation of resolved gas structures and kinematics in high angular resolution images is often ambiguous due to the blending of structures, and the confusion of motions from, for example, infall, outflows and rotation. Determination of the chemical composition may provide independent constraints, aiding in distinguishing distinct gas components (e.g. Liu et al. 2015) and potentially inferring the evolutionary status or evolutionary history (e.g. van Dishoeck 2009). For example, a number of recent observations of HMSFRs have been made on both large scales ($> 10^5$ AU; e.g. Foster et al. 2011; Sanhueza et al. 2012; Hoq et al. 2013; Jackson et al. 2013; Gerner et al. 2014) and small scales (< 2000 AU; e.g. Orion-KL within 1′, Feng et al. 2015; AFGL 2591, Jiménez-Serra et al. 2012; infrared dark clouds (IRDC) G11.11-0.12 Wang et al. 2014) with the aim of classifying their different evolutionary phases. While observations on the larger spatial scales are useful to characterize the general properties of the entire clump, high angular resolution observations ($\lesssim$2000 AU scales) can probe in more detail the processes associated with HMSFRs, such as hierarchical fragmentation and chemical evolution.

The focus of the present paper is a comprehensive study of the internal chemical segregation in two HMSFRs: NGC 7538 S and IRS1. Both sources have been the subject of a kinematical study (Beuther et al. 2012, see Section 2). In the following discussion we adopt the nomenclature of Zhang et al. (2009), where the authors refer to gas structures according to their char-

Send offprint requests to: syfeng@mpe.mpg.de

acteristic spatial scales. A gas "clump" is defined as a structure that has > 1 pc size (e.g. the entire region of NGC 7538); a "core" refers to a structure on the size scale of ~ 0.1 pc, which may contain or will form a small stellar group (e.g. NGC 7538 S and IRS1); and "condensations" are internal substructures in a gas core, which have ~ 0.01 pc size and will likely form a single star or multiple-star system.

Several evolutionary schemes have been suggested to describe the early phases of HMSFRs (e.g. Beuther et al. 2007; Zinnecker & Yorke 2007; Tan et al. 2014). These schemes, however, are mainly based on the study of the physical conditions (density, temperature, spectral energy distribution, kinematics, etc.). Our work focusses on the interpretation of the observed chemical composition and a comparison with chemical modelling to improve upon the HMSFR evolutionary sequence proposed by Gerner et al. (2014). We note that the observations of Gerner et al. (2014) have a 10^5 AU spatial resolution, thus each region in their sample corresponds to an unresolved core. Therefore, chemical properties (e.g. spectral line feature, temperature, and molecular abundance) on that scale are dominated by the most chemically evolved, embedded condensation(s), i.e. NGC 7538 S and IRS1 show chemical properties dominated by hot molecular cores (HMCs). In the following discussion, we consider high-mass protostellar objects (HMPOs) and HMCs as condensations.

Characteristics of each evolutionary stage are briefly summarized as follows:

(1) Prestellar objects are formed in cold and dense molecular cores. Examples of these cores are usually detected in Bok globules or IRDCs. At this particular stage, many molecules are forming or have already formed via rapid ion-molecule gas-phase reactions, followed by slower molecular freeze-out and surface processes. From chemical point of view, it makes sense to designate the onset time of molecular formation as the starting point $t = 0$, which likely precede the formation of the dense cores themselves. This particular time moment is very difficult to estimate for any given observed environment but, given relatively short timescale of high-mass star formation (e.g. Russeil et al. 2010; Tackenberg et al. 2012), it should not be much longer than the typical IRDC lifetime of $\sim 10-5\times10^4$ yrs.

(2) Gravitational collapse leads to the formation of the HMPOs and subsequently compact HMCs. The masses of these embedded protostars have increased to over 8 $M_\odot$ and exhibit a temperature of hundreds of Kelvin even at the scale of 0.01 pc. The chemical complexity of these regions, characterized by the presence of complex organic molecules (COMs[1]), is driven predominantly by the hot gas component. Although a clear chemical distinction between the HMPO and HMC phases has not yet been observed, the number and intensity of molecular transitions are higher in HMCs than in HMPOs. Furthermore, outflows and shocks associated with HMPOs and HMCs would be expected to enhance the abundance of certain molecules (e.g. sulfur-bearing species) which would provide for an observational discriminant.

(3) Formation of more complex molecules continues as the HMC evolves until the molecules are photo-dissociated by the energetic UV-radiation of young stars. HMSFRs at this stage may start to exhibit ultra-compact HII (UCHII) regions.

In this paper, some background on the target sources is provided in Section 2. A brief summary of our observations is given in Section 3 and the full-bandwidth spectra are presented in Section 4. Analysis of chemical abundances and the results of 1-D radiation transfer modelling are presented in Sections 5 and 6, respectively. Finally, the results are discussed in Section 7, and the conclusions are presented in Section 8.

2. Targets

The molecular cloud NGC 7538 is located in the Perseus arm of our Galaxy at a distance of 2.65 kpc (Moscadelli et al. 2009). Associated with an optically visible HII region, this region harbors several clusters of infrared (Martin 1973; Wynn-Williams et al. 1974) and radio continuum sources (Campbell & Thompson 1984). At least three dense gas cores (IRS1, IRS9, and S) hint at the presence of (proto-)stellar accretion disks which are driving powerful molecular outflows (e.g. De Buizer & Minier 2005; Kraus et al. 2006; Sandell & Wright 2010; Barentine & Lacy 2012; Beuther et al. 2012, 2013).

Previous studies proposed a sequential evolution of these dense cores, where the "older" IRS1 lies in the northwest, and the "younger" S lies in the southeast (Elmegreen & Lada 1977; Werner et al. 1979; McCaughrean et al. 1991; Ojha et al. 2004; Balog et al. 2004; Qiu et al. 2011). Therefore, a comparison of the chemical compositions of IRS1 and S (hereafter, NGC 7538 S in case of confusion) regions, is important to demonstrate a chemical evolutionary sequence. In addition, our high angular resolution observations may further unveil the sequential chemical evolution of their internal structures.

IRS1 is the brightest millimetre (mm) continuum source in the molecular cloud NGC 7538 (Scoville et al. 1986). Its systemic velocity is $V_{lsr} = -57.4$ km s^{-1} (van der Tak et al. 2000; Sandell et al. 2009). A hyper-compact HII (HCHII) region is present, which may be ionized by a O6 / O7.5 type (8×10^4 $L_\odot$, 30 $M_\odot$, Werner et al. 1979; Campbell 1984; Akabane & Kuno 2005) host star. Previous millimetre observations of HCO^+ and HCN line emission in the central 1′ area (Pratap et al. 1989) have revealed a 10″–20″ scale shell-like structure ($V_{lsr} \sim -56.5$ kms^{-1}). Observations of infrared absorption by dust grains and icy mantles have probed an exterior cool gas envelope on ~72,000 AU scale (Willner 1976; Willner et al. 1982; van der Tak et al. 2000; Zheng et al. 2001; Gibb et al. 2004). Observations of NH_3 absorption ($V_{lsr} \sim -60$ kms^{-1}) against the HCHII region have detected warmer gas in the inner region (Wilson et al. 1983; Henkel et al. 1984; van der Tak et al. 2000; Goddi et al. 2015). Numerous maser sources have been detected within the central 1,000 AU: some outline two small-scale knotty outflows (e.g. OH, H_2O, NH_3, CH_3OH, and H_2CO; Gaume et al. 1991, 1995; Hutawarakorn & Cohen 2003; Hoffman et al. 2003; Kurtz et al. 2004), while the rest may trace the rotational motion (CH_3OH, Pestalozzi et al. 2004, 2009; Beuther et al. 2012, 2013).

[1] Carbon-bearing molecules containing ≥ 6 atoms, which are theoretically sublimated from grain to the gas phase or produced via ion-molecular reaction in the gas phase as temperature increases (Garrod et al. 2008).

NGC 7538 S is an extended (~0.2 pc) source located 80″south of IRS1. It is less luminous than IRS1 (1.3×10^4 $L_\odot$, Sandell et al. 2003) and is considered to be the "youngest" star-forming core in NGC 7538. Weak mm free-free emission (Sandell & Sievers 2004; Pestalozzi et al. 2006; Zapata et al. 2009), H_2O masers, OH masers, CH_3OH masers, and optically thick thermal lines have been detected in the high gas column density region (Sandell & Wright 2010). Mapping the molecular lines and dust continuum emission has inferred an embedded, $10 - 100$ $M_\odot$ young star or star cluster (Corder 2009; Wright et al. 2012; Naranjo-Romero et al. 2012; Beuther et al. 2012), which is associated with the gas accretion flow or disk, and the driving of a compact (0.2 pc), molecular outflow (Beuther et al. 2012; Wright et al. 2014). High angular resolution observations of SiO line emission have resolved at least two collimated bipolar outflows (Corder 2009; Naranjo-Romero et al. 2012).

3. Observations

Here were summerize the observational parameters which are directly relevant to the following chemical study. For a full details of the PdBI 1.37 mm observations and data reduction, we direct the reader to Beuther et al. (2012).

The observations were carried out in the A and B array configurations on Jan. 26, 2011 and Feb. 10, 2011, respectively. The baselines range from 88 m to 760 m with 6 antennas, filtering out structures with an extent > 5,100 AU. The phase referencing centers of our target sources are $\alpha_{2000} = 23^h13^m45.36^s$, $\delta_{2000.0} = 61^o28'10.55''$ (IRS1), and $\alpha_{2000} = 23^h13^m44.86^s$, $\delta_{2000.0} = 61^o28'48.10''$ (NGC 7538 S). Observations of target sources were interleaved with the observations of quasars 2146+608, 0059+581, and 0016+731 for the gain phase and amplitude calibrations. We observed 3C345, 3C273, and MWC349 for passband calibration and absolute flux referencing. We note that the typical absolute flux accuracy of PdBI observations is ~20%.

We configured the WIDEX correlator to cover in two polarizations with a the frequency range 217.167– 220.836 GHz and an uniform spectral resolution of 1.9 MHz (2.66 km s^{-1}). This spectral resolution is coarse for kinematical studies; nevertheless is adequate for our primary purpose of probing the chemical evolution. We extracted the continuum data of NGC 7538 S from the spectral line-free channels.

IRS1 exhibits extremely rich spectral line emission, such that the continuum data derived from the spectral line-free channels have a poor S/N. Thus, the continuum image of IRS1 was produced by averaging over all available spectral channels. A quantitative comparison of the continuum images of IRS1, with and without line contamination shows little difference, suggesting that spectral line emission in IRS1 does not seriously contaminate the continuum image. Spectral line contamination is discussed in Beuther et al. (2012).

The continuum image of NGC 7538 S achieves an 1σ rms noise level of 0.94 mJy beam^{-1} while for IRS1 it is dynamic range limited with a 1σ rms noise level of 22 mJy beam^{-1}. The achieved 1σ rms noise levels for each 2.66 km s^{-1} wide spectral channel, are 2.8 mJy beam^{-1} and 26 mJy beam^{-1} for NGC7538 S and IRS1, respectively.

Data calibration and imaging was carried out using the CLIC[2] and MAPPING[3] software packages. The images were generated adopting a "robust" weighting scheme, and the Clark algorithm (Clark 1980). The synthesized beams are $\sim 0.40'' \times 0.36''$ for IRS1 and $\sim 0.57'' \times 0.37''$ for NGC 7538 S, which correspond to a spatial resolution of $\sim 1,100$ AU at the assumed source distance of 2.65 kpc.

4. Observational results

4.1. Continuum emission

Figure 1 presents the 1.37 mm continuum images of NGC 7538 S and IRS1. We have resolved several compact substructures, consistent with previous observations (e.g. Naranjo-Romero et al. 2012; Wright et al. 2012; Beuther et al. 2012; Zhu et al. 2013; Wright et al. 2014). The nominal absolute positions, peak specific intensity per beam of the internal substructures, and the projected size of the internal condensations from 2-D Gaussian fits, are summarized in Table 1.

NGC 7538 S is resolved into three compact condensations (hereafter MM1, MM2, and MM3; see Figure 1) along the NE-SW direction, which have nearly identical continuum peak specific intensities. The most extended condensation, MM1, may be resolved into multiple internal substructures, tentatively identified as 1a, 1b, and 1c. MM1-1a and 1b have been detected by previous 1.2″resolution 1.3 mm observations using the Submillimetre Array (SMA, Sandell & Wright 2010; Naranjo-Romero et al. 2012), and the previous 1.4 mm/3 mm observations using the CARMA/BIMA array (Wright et al. 2012; see Table 1 for corresponding observations). MM1-1c has been reported by the previous SMA observations in Naranjo-Romero et al. (2012), but was undetected by the CARMA observations in Wright et al. (2012), most likely because of insufficient sensitivity. We note that MM1-1a and 1b, with an 0.5″projected separation, are associated with a heavily obscured mid-IR counterpart (Spitzer IRAC and IRS data, Wright et al. 2012), suggesting they may be more "evolved" than the other compact-mm condensations.

In addition, MM1 was suggested to be the driving source of a 0.1–0.4 pc scale, ionized bipolar outflow (Sandell & Wright 2010)[4], which is perpendicular to the major axis of the proposed edge-on disk (Sandell et al. 2003). However, this ionized outflow shows no clear continuum detection in our observations, likely because the emission is primarily over extended angular scales and therefore is filtered out due to missing short-spacing data. We mark this ionized outflow as JetN and JetS in Figure 1.

At 1.37 mm, the continuum peak flux specific intensity of IRS1 is ~60 times higher than that of NGC 7538 S. Our observations, with a spatial resolution of ~1,100 AU, do not find internal substructures towards IRS1, however we do detect a companion in the southwest (IRS1-mmS, hereafter) with a

[2] http://www.iram.fr/IRAMFR/GILDAS/doc/html/clic-html/clic.html

[3] http://www.iram.fr/IRAMFR/GILDAS/doc/html/map-html/map.html

[4] The outflow has been detected by previous VLA observations (Sandell & Wright 2010) coninciding with an OH maser (Argon et al. 2000), a Class II CH_3OH maser (Pestalozzi et al. 2006), and a cluster of H_2O maser spots (Kameya et al. 1990).

Table 1: Properties of continuum substructures in IRS1 and NGC 7538 S, identified in Figure 1.

Source		R.A. [J2000] 23^h13^m	Dec. [J2000] 61°	Peak Flux I_ν (mJy/beam)	Size (θ^d) ($'' \times ''$, PA°)	T_{rot} (K)	$N^{e,g}_{H_{2,1}}$ (10^{23}cm^{-2})	$N^{f,g}_{H_{2,2}}$ (10^{23}cm^{-2})	M^m ($M_\odot$)	Alternative Designations
IRS1	IRS1-peak	$45^s.4$	$28'10''.4$	1945.1 ± 182.3	$0.49'' \times 0.43''$, 13°	214 ± 66^h	$--^k$	44.07 ± 31.51	$--^k$	
	IRS1-mmS	$45^s.3$	$28'09''.8$	126.4 ± 3.1	$0.61'' \times 0.37''$, 87°	162 ± 14^i	$--^k$	$--^l$	$--^k$	SW extension[a]
S	MM1	$45^s.0$	$26'49''.8$	32.2 ± 1.1	$0.87'' \times 0.64''$, 153°	172 ± 23^i	16.90 ± 2.52	16.50 ± 1.91	3.28 ± 0.52	1a:SMA3[b],CARMA S_{A1}[c] 1b:SMA4[b],CARMA S_{A2}[c] 1c:SMA5[b]
	MM2	$44^s.7$	$26'48''.7$	25.7 ± 0.8	$1.08'' \times 0.59''$, 166°	137 ± 14^i	17.05 ± 2.11	2.70 ± 0.19	2.54 ± 0.30	2:SMA2[b], S_B[c]
	MM3	$44^s.5$	$26'47''.8$	27.0 ± 1.1	$0.68'' \times 0.49''$, 170°	50^j	52.49 ± 2.14	0.29 ± 0.01	≤ 6.58	3:SMA1[b], S_C[c]
	JetN	$44^s.7$	$26'52''.1$	$\sigma = 0.12$	$--$	150^j	≤ 0.27	2.54 ± 0.01	$--$	
	JetS	$45^s.2$	$26'48''.4$	$\sigma = 0.27$	$--$	150^j	≤ 0.61	3.33 ± 0.03	$--$	

Note. *a.* Zhu et al. (2013).
b. Naranjo-Romero et al. (2012).
c. Wright et al. (2012).
d. Projection size is fitted with 2-D Gaussian
e. H_2 column densities are calculated from the continuum using Eq. 1. The uncertainties come from the measurement of the continuum fluxes and the calculation of temperatures.
f. H_2 column densities are calculated from $C^{18}O$ conversion. The uncertainties come from the gaussian fit to $C^{18}O$ ($2 \rightarrow 1$) and the excitation temperatures.
g. The column density estimates in MM1–MM3 from dust continuum are thought more reliable than that derived from $C^{18}O$ conversion (see Appendix C.3) .
h. Temperature lower limit is taken by assuming the same as in IRS1-mmS, and upper limit is taken from Goddi et al. (2015) (see details in Section 5.1).
i. Temperature derived from rotation diagram of CH_3CN in Figure 4.
j. Temperature assumed based on estimation from Sandell & Wright (2010).
k. Continuum is dominated by free-free emission at 219 GHz.
l. Column density could not be obtained because $C^{18}O$ ($2 \rightarrow 1$) shows P-Cygni profile.
m. Mass on scale of 0.01 pc is derived from Eq. 2, based on total flux reported in Beuther et al. (2012), which is corrected for free-free contribution and with > 90% missing flux.

S/N > 5.

IRS1-mmS has also been detected by previous 0.7″resolution mm continuum observations using the SMA and CARMA (Zhu et al. 2013). However, the source was detected neither at 1.4 cm by e.g. Moscadelli et al. (2009), nor in high angular resolution observations (0.2″, ∼ 500 AU) at 843 μm by Beuther et al. (2013), which have resolved at least three substructures embedded within IRS1.

4.2. Spectral line

4.2.1. Line identification

We produced image cubes covering the full available bandwidth (∼4 GHz). The beam-averaged spectra at the peaks of the gas substructures we identified in the 1.37 mm continuum images (Table 1), are given in Figure 2.

We identify molecular species based on the spectra of MM1 and the IRS1-peak, which exhibit the strongest line emission. We caution that our line identifications are limited by the blending of multiple velocity components, the broad linewidths and the limited (∼ 2.7 km s^{-1}) velocity resolution of our observations. We have cross-compared our results with higher velocity resolution (∼ 1.2 km s^{-1}) spectra of Orion-KL (Feng et al. 2015) and have verified that the identified molecular species are indeed expected. We have used a synthetic spectral fitting program (Sanchez-Monge 2011; Palau et al. 2011) incorporating molecular data from the JPL[5] and CDMS[6] catalogues, to simultaneously fit multiple lines. The fits are based on the assumptions that all transitions are optically thin, are in local thermodynamic equilibrium (LTE), and have the same linewidth[7]. This approach is particularly suited for self-consistently identifying multiple transitions of a certain molecular species (e.g. Fig. A1).

We have identified over 90 molecular lines, which are summarized in Table A1. We mark tentative identifications of some weak lines (∼ 3σ rms) with symbol "*", and mark the brightest transition of each species with "†". We find large spectral variations within both NGC 7538 S and IRS1.

NGC 7538 S shows numerous molecular lines. The three internal condensations, separated by less than 2″, display nearly identical continuum peak specific intensities however show differences in their line spectra. MM1 exhibits the strongest intensity for majority of line emission. We only detect weak OCS ($O^{13}CS$), ^{13}CO ($C^{18}O$), and CH_3OH line emission (where we consider a "detection" if the line emission is $\geq 4\sigma$ rms) from MM3.

In addition, we have detected outflow/shock tracers, such as H_2CO ($H_2^{13}CO$), CH_3OH, SO, OCS, and $C^{18}O$ (^{13}CO), around

[5] http://spec.jpl.nasa.gov (Pickett et al. 1998)
[6] http://www.astro.uni-koeln.de/cdms/catalog (Müller et al. 2005)
[7] The synthetic fitting program we use here is for line detection, but not for finding the best fit of column density or temperature. The optically thin assumption may break down for certain molecular transitions, which leads to some line intensity deviations between the synthetic spectra and the observational results.

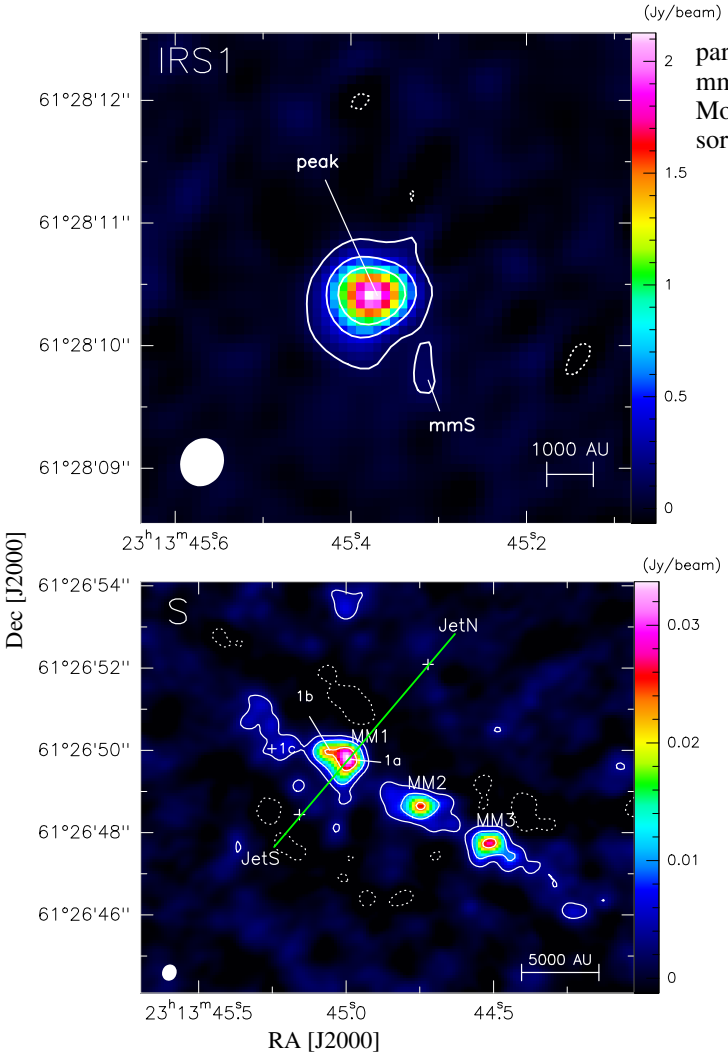

Fig. 1: Colormaps and contours of the continuum emission obtained with the PdBI at 1.37 mm. Line emission was removed for NGC 7538 S and shown to be negligible for IRS1 (see text). For IRS1 (*upper panel*), the white solid contours start at 5σ and continue in 20σ steps ($\sigma = 22$ mJy beam^{-1}). For NGC 7538 S (*lower panel*), the contour levels start at 4σ and continue in 10σ steps (σ = 0.94 m Jy beam^{-1}). Dashed contours represent negative emission at the same level as the solid (positive) contours. The synthesized beams are shown at the bottom left of each panel. The direction of the studied outflow is shown with a green line. Labels mark individual substructures we identified.

the MM1-outflow(s) (i.e. JetN, JetS), despite the low local gas column density. We note that these lines are brighter around the outflows than MM3.

Unlike NGC 7538 S, the spectrum of IRS1-peak exhibits numerous absorption lines. Some of these lines (e.g. HC_3N, HNCO, SO_2, and $C^{18}O$) display P-Cygni profiles, suggesting they may be associated with jets or outflows. Additionally, other lines (e.g. CH_3OH, OCS, and NH_2CHO) show inverse P-Cygni profiles, indicative of gas infall (Beuther et al. 2012). We also detect four strong emission lines marked as "?CH_3OCH_3" and "?CH_3OH". We discuss the tentative identification of these lines and their unique properties in Section 7.3.

We detect more lines in IRS1-mmS than in MM1–MM3. In particular, multiple lines of $HCOOCH_3$ are detected in IRS1-mmS but are absent in MM1–MM3 or JetN(S) (Figure A1). Moreover, in IRS1-mmS $C^{18}O$ and ^{13}CO are observed in absorption, but the other lines are observed in emission (Figure 2).

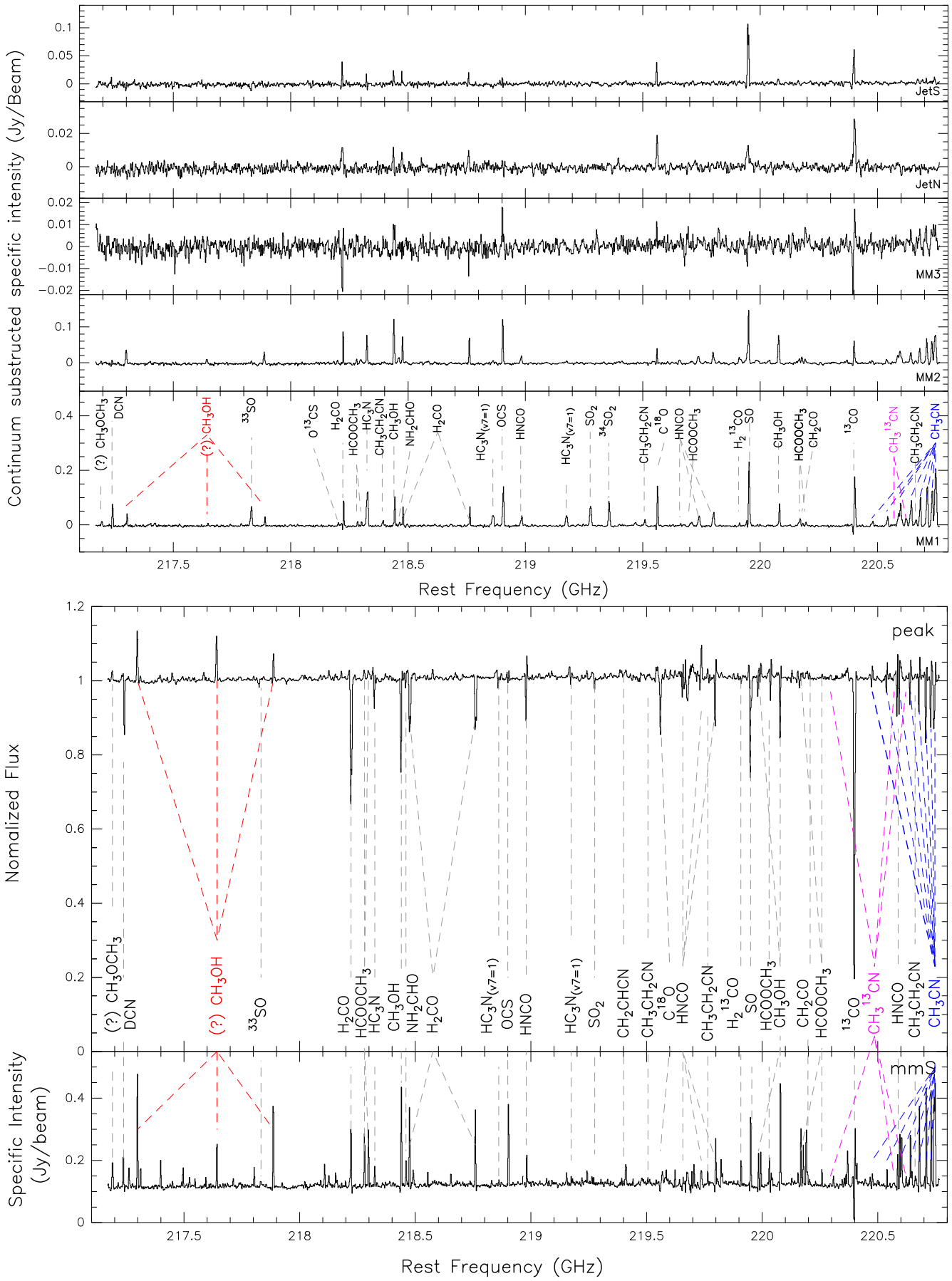

Fig. 2: Spectra extracted from positions denoted in Figure 1 after imaging the whole data cube. All strong lines are labeled; the identification of lines marked with"?" is tentative (see Section 7.3). Continuum-subtracted spectra from different substructures in NGC 7538 S are shown in the *upper panel*, while the *lower panel* presents continuum-unsubstracted spectra from two positions in IRS1 (the spectrum of IRS1-mmS shows the continuum level). All of the detected $HCOOCH_3$ transitions are shown in Figure A1.

4.2.2. Line Imaging

Identified molecular lines listed in Table A1 can be attributed to 15 different species (and 22 isotopologues thereof). In the following discussion, molecular lines observed from IRS1-mmS is beyond the scope of this paper, given its uncertain nature in 1.37 mm continuum emission. For NGC 7538 S, we present the strongest, unblended transitions of each isotopologue (marked as "†" in Table A1) as intensity maps in Figure 3. The intensities are integrated over a velocity range[8] as marked in Figure A2, to enhance the contrast of the images.

Different molecular species have distinct spatial distributions (as in Figure 3), although most display emission peaks around MM1 and (or) MM2. We note that our observations are not sensitive to emission on angular scales larger than $\sim 2''$ due to filtering and therefore cannot recover all of the line emission from the extended structures, e.g. outflows.

Most of the isotopologues (19 out of 22) peak at MM1 with line center velocities around $V_{lsr} \sim -60$ km s^{-1}. Of these, SO, H_2CO, CH_3OH, and ^{13}CO aditionally exhibit strong emission even in MM1-1c. Of all these species peaking towards MM1, several COMs (e.g. CH_3CN, $CH_3^{13}CN$, and CH_3CH_2CN) are indicative of high temperatures. Furthermore, the presence of vibrationally-excited HC_3N ($v_7 = 1$) lines indicates mid-IR pumping, and hence suggests the existence of a hot embedded IR-emitting source. Combined, these molecular distribution peaks suggest that MM1 is a HMC.

MM2 shows $> 4\sigma$ emission from $C^{18}O$ and ^{13}CO lines, as well as from only the main isotopologue lines of the other species with a $V_{lsr} =\sim -58$ km s^{-1}. These lines have typically lower specific intensities observed in MM2 than in MM1. Most of these species evaporate from the grain surface early in the warm-up phase, such as CH_3OH, $HCOOCH_3$, and HNCO, and our observations did not cover their rare isotopologue lines. Minority of these species are OCS, SO, and CH_3CN; their rare isotopologue lines are observed but exhibit $< 4\sigma$ emission.

Unlike the majority of species described above, lines of CH_2CO and NH_2CHO are stronger in MM2 than in MM1. In addition, the only $H_2^{13}CO$ line ($3_{1,2} \rightarrow 2_{1,1}$) exhibits stronger emission in MM2 than in MM1, which is on contrary to the MM1-dominated emission of the H_2CO lines ($3_{2,2} \rightarrow 2_{2,1}$, $3_{2,1} \rightarrow 2_{2,0}$, and $3_{0,3} - 2_{0,2}$).

5. Source temperatures and chemical variations

We derive the spatial variations of gas temperature, molecular column density, and molecular abundance in order to diagnose the chemical evolution at core scale from IRS1 to NGC 7538 S, and at condensation scale with the condensations MM1–MM3.

5.1. Temperature

A comprehensive chemical model should not only reproduce the observed chemical composition, but should also be based on realistic assumptions of gas temperature and density.

[8] This range is slightly larger than the FWHM of each line in order to account for the small variation in the peak velocity between different substructures.

Our sources show high gas number densities (see discussion in Section 5.2.2), so collisions are sufficient to thermalize rotational levels, thereby making the rotational excitation temperature (T_{rot}) a good approximation to the kinetic temperature. *Rotational diagrams* provides the simplest method to deriving gas temperatures, when multiple (> 3) transitions with different upper state energy levels E_u/k of an isotopologue have been observed. This method cannot be simply applied to IRS1-peak due to the confusion with the absorption lines, however we have derived the rotational diagrams of multiple species for MM1, MM2, and IRS1-mmS from their emission lines, as discussed below:

- **CH_3CN** line forests are regarded as good thermometres for dense molecular gas (Boucher et al. 1980; Wright et al. 1995). However, if the emission lines are optically thick then the estimated T_{rot} can significantly exceed T_{kin}. This can be circumvented using optically thin lines of less abundant isotopologues, e.g. $CH_3^{13}CN$. In our observations most $CH_3^{13}CN$ transitions are blended with the adjacent molecular transitions, except for $CH_3^{13}CN$ ($12_2 \rightarrow 12_2$). Therefore, we estimate an opacity corrected T_{rot} using the optically thick CH_3CN lines for MM1, MM2, and IRS1-mmS (panels 3–5 of Fig. 4). See Appendix A (also in Feng et al. 2015) for more details on this iterative approach.

  We assume that all $K = 1 - 8$ components have the same linewidth in each individual substructure. Although K=0, 1 lines are blended, they have similar relative intensity and E_u/k and therefore, weighting the measured intensity relative to the expected relative intensity for each component yields the individual integrated-intensities of each line. Solid and dashed lines in Panels 1–2 of Figure 4 show the best synthetic spectrum fits with or without, respectively, opacity correction for CH_3CN ladder in MM1 and IRS1-mmS. Panels 3 and 5 show the corresponding rotation diagrams. We find T_{rot} derived without opacity correction is overestimated by a factor of 1.5–2, leading to an underestimation of the CH_3CN column densities by a factor of 3–5.

- **HNCO** has four detected transitions in our observations, with E_u/k ranging from 50 K– 450 K. The rotational temperatures derived from HNCO are consistent with those derived from CH_3CN in MM1 and IRS1-mmS, however slightly higher than from CH_3CN in MM2. Such differences in T_{rot} between CH_3CN and HNCO is also observed at larger scales (e.g. Bisschop et al. 2007). Possible explanations include: (1) The excitation of HNCO may be dominated by radiative processes rather than collisional (Churchwell et al. 1986); (2) Our frequency resolution does not allow us to resolve blended hyperfine components[9] which may not be in LTE (Panel 9 of Figure 4); (3) Limited by angular resolution, we cannot distinguish whether HNCO and CH_3CN trace the same gas components in MM1 – MM3; and (4) The optically thin assumption may break down for HNCO, in particular in MM2.

- H_2CO is routinely used as a thermometre for dense gas (Mangum & Wootten 1993; Ao et al. 2013). However, as

[9] Two pairs of twin lines $10_{3,8} \rightarrow 9_{3,7}$–$10_{3,7} \rightarrow 9_{3,6}$ and $10_{2,9} \rightarrow 9_{2,8}$–$10_{2,8} \rightarrow 9_{2,7}$ are blended and contain further hyperfine splittings. Each pair of lines has the same relative intensity and E_u/k. Therefore, the rotation diagram is based on the assumption that each line have the same contribution to the blending intensity integration.

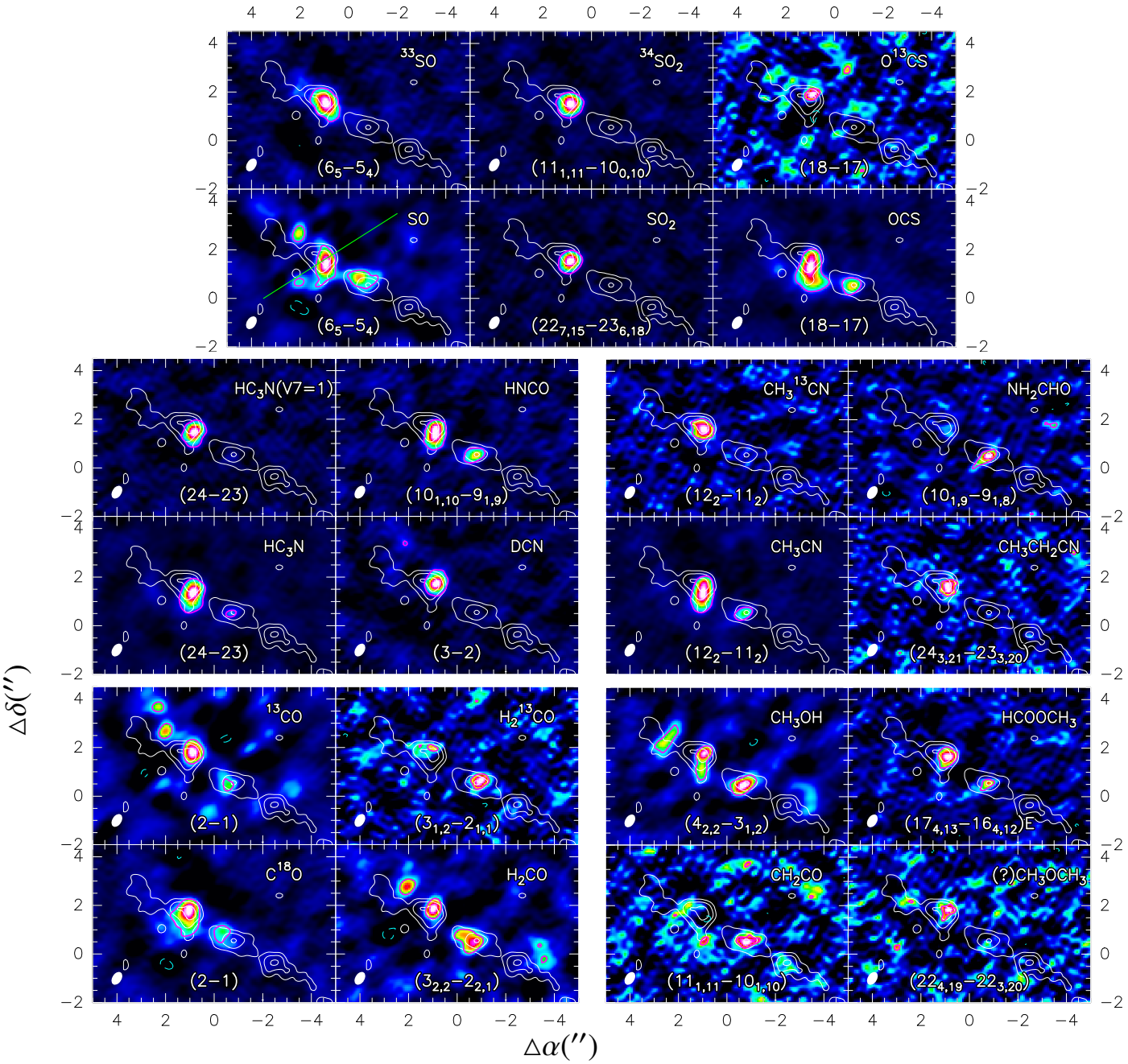

Fig. 3: Maps of the strongest line from each isotopologue detected in PdBI observations at 1.37 mm. The intensities have been derived by integrating the line emission over the velocity range shown in Figure A2. The synthetic beam is shown at the bottom left of each panel. White contours show the continuum (at 4σ, 14σ, and 24σ levels with $\sigma = 0.94$ m Jy beam^{-1}), purple contour reveals the region where molecular specific intensity $> 3\sigma$, and the dashed green contour reveals the negative specific intensity beyond -3σ because of the interferometric side lobe effect. Green lines in the SO map sketch the outflow directions. All images have different color scales (in mJy beam^{-1} km s^{-1}), increasing from black to white, which are optimized to emphasize the features in the distribution of each line.

shown in Panel 11 of Figure 4, the data are not consistent with optically thin emission. Without any clear opacity correction, we cannot use this transitions for further temperature estimates.

– **Other species**: The three CH_3CH_2CN transitions observed have approximately the same E_u/k and therefore cannot provide accurate constraints for T_{rot}. Several transitions of $HCOOCH_3$ were covered as well, however, were mostly only marginally detected (Table. A1). We detected five CH_3OH transitions. Three of the CH_3OH may be masing (see Section 7.3), including two in the torsionally excited state (Table 5), such that they cannot constrain T_{rot}.

In the following, we assume that the CH_3CN rotational temperatures in MM1–MM2 and IRS1-mmS are equal to the gas

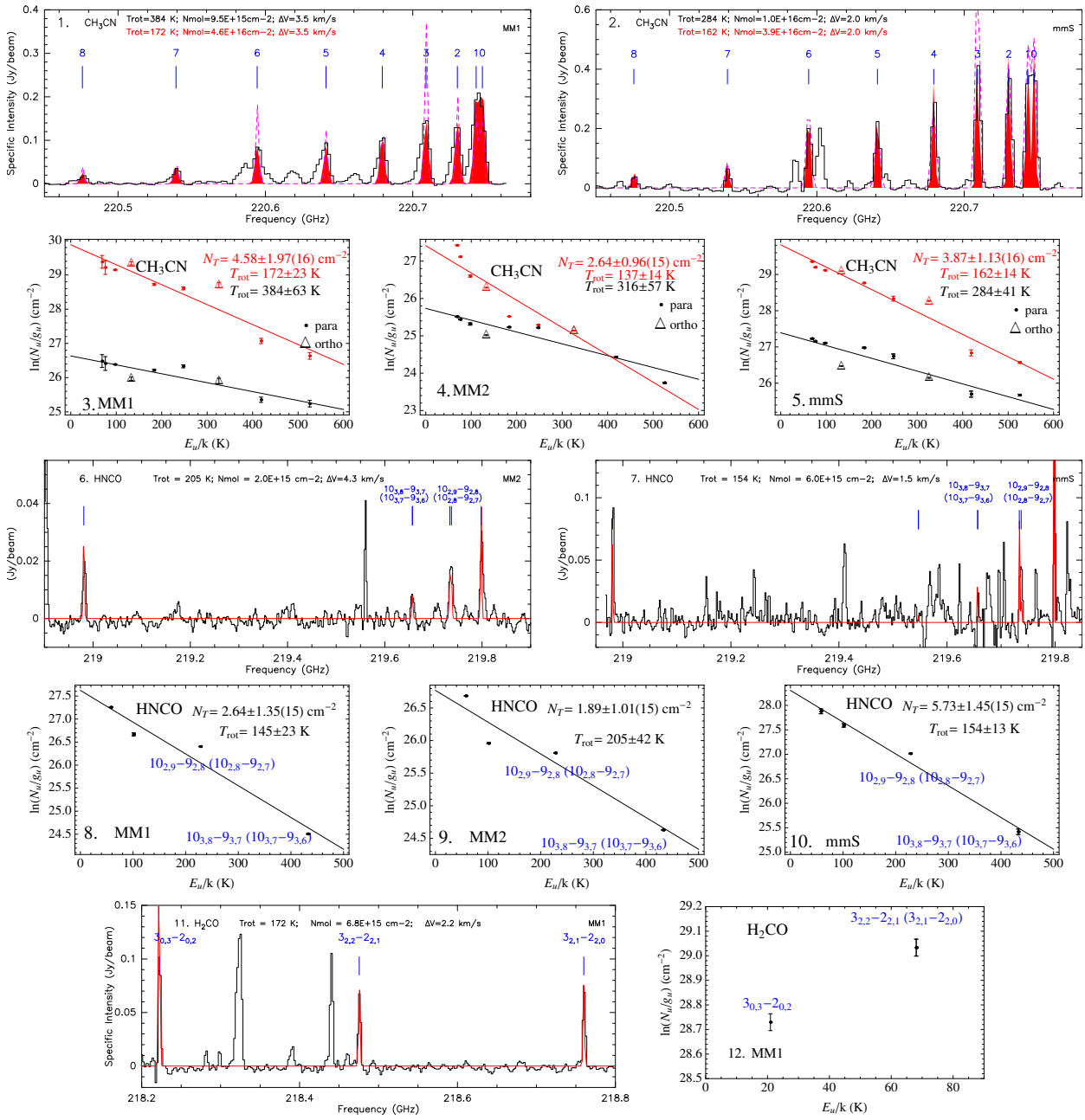

Fig. 4: Rotation diagrames and synthetic spectrum fits of CH_3CN, HNCO, and H_2CO in MM1 (or MM2) and IRS1-mmS. Panels 1–2 present the CH_3CN spectra towards MM1 and IRS1-mmS in black, fitting with optically thin assumption in dashed purple, and fitting with opacity correction in filled red. Panels 3–5 show the rotation diagrams of CH_3CN derived for MM1, MM2, and IRS1-mmS, with black dots and fits corresponding to the optically thin assumption, whereas red dots and fits include correction for opacity. Panels 6–7 present the HNCO (assumed optically thin) synthetic spectrum fits towards MM2 and IRS1-mmS, with blended lines marked (fit in red). Panels 8–10 show the rotation diagrams of HNCO (assumed optically thin). Panel 11 presents the H_2CO synthetic spectrum fits towards MM1. Panels 12 shows the data points of H_2CO lines in MM1, which cannot be fitted in the rotation diagram. The estimated T_{rot} and molecular column density from each rotation diagram is indicated in each panel. Errors are derived from scatter in the data points.

kinetic temperature. Given that CH_3CN in MM3 and the outflow regions are observed at $< 3\sigma$, and each detected species in these regions present only one line, we are unable to directly measure the gas temperature. Therefore, we assume that temperatures in JetN and JetS are $\sim$ 150 K following Sandell & Wright (2010) (147 ± 40 K). In MM3 the gas temperature must be large enough to excite $> 3\sigma$ line emission from CH_3OH ($4_{2,2} \rightarrow 3_{1,2}$, E_u/k = 46 K), while also being lower than in MM1–MM2 because of the smaller number of lines and their lower intensities. We assume the gas temperature of MM3 to be $\sim$ 50 K which is comparable with that of the associated, more extended gas envelope as constrained by the previous observations of $H^{13}CN$, DCN, and CH_3CN (52 ± 10 K, Sandell & Wright 2010). Toward IRS1-peak, we take the gas temperature measured from

IRS1-mmS as the temperature lower limit, and that measured by Goddi et al. (2015) at 0.15″–0.3″resolution as the temperature upper limit.

5.2. Column densities

5.2.1. Spectral line:

We assume that all transitions are in LTE to calculate column densities from integrated intensities of the strongest transition for each isotopologue (see Appendix B).

For several species where we have additionally detected their rare isotopologue lines, e.g. SO ($6_5 \rightarrow 5_4$)- ^{33}SO ($6_5 \rightarrow 5_4$), OCS ($18 \rightarrow 17$)- O^{13}CS ($18 \rightarrow 17$), ^{13}CO ($2 \rightarrow 1$)- C^{18}O ($2 \rightarrow 1$) and $CH_3^{13}CN$ ($12_2 \rightarrow 11_2$)- CH_3CN ($12_2 \rightarrow 11_2$), we have derived the molecular column densities assuming an opacity correction (Eqs B.8–B.10). We find τ = 3–45 (see Table C.1), indicating that the lines are very optically thick. For the remaining species we assume that the observed transitions are optically thin, an assumption discussed in Appendix C.2.

Tables A4–A6 and Figure 5 summarize the derived beam-averaged column densities of 22 isotopologues. Column densities vary significantly between the substructures. Most present a decreasing trend from MM1 to MM3, with the exceptions of NH_2CHO, $H_2^{13}CO$, and CH_2CO. Given the similar sizes and the 1.37 mm continuum emission intensities of MM1–MM3, the observed decreasing column densities are likely because of chemical segregation.

5.2.2. Continuum:

In NGC 7538 S, the 1.37 mm continuum emission is dominated by thermal dust emission. Observations of Wright et al. (2012) have shown that the contribution from the free-free emission is negligible. Assuming that the dust emission at mm wavelength is optically thin and that the temperature of the dust and gas temperatures are equal, we are able to calculate the H_2 column densities and masses for different substructures. Following Hildebrand (1983) and Schuller et al. (2009),

$$N_{H_2} = \frac{I_\nu R}{B_\nu(T_{dust})\Omega_a \kappa_\nu \mu m_H} \quad (cm^{-2}) \tag{1}$$

$$M = \frac{S_\nu R D^2}{B_\nu(T_{dust})\kappa_\nu} \quad (g) \tag{2}$$

where I_ν is the peak specific intensity for each substructure (in Jy/beam, taken to be the 3σ upper limit for the outflow regions), S_ν is the total flux (in Jy, free-free contribution excluded), measured within 4σ contours (Beuther et al. 2012), R is the gas to dust mass ratio (taken to be 150 from Draine 2011), $B_\nu(T_{dust})$ is the Planck function for a dust temperature T_{dust}, Ω_a is the solid angle of the PdBI beam (in rad^2), μ is the mean molecular weight of the ISM, assumed to be 2.33, m_H is the mass of an hydrogen atom (1.67×10^{-24} g), and D is the source distance. We assume a model of agglomerated grains with thin ice mantles[10] for densities 10^8 cm^{-3} in MM1–MM3[11], and 10^6 cm^{-3} in JetN and JetS[12], yielding a dust absorption coefficient at 1.37 mm of κ_ν = 0.77 cm^{2}g^{-1} in MM1–MM3, and κ_ν = 0.62 cm^{2}g^{-1} in JetN (S) (interpolation from Ossenkopf & Henning 1994).

We find peak column densities for the substructures in NGC 7538 S are similar $(1-5) \times 10^{24}$ cm^{-2} ($N_{H_{2,1}}$ in Table 1). The outflow regions have the lowest column densities which may be underestimated potentially because of the lack of short-spacing data.

The 1.37 mm continuum in IRS1 is dominated by free-free emission (e.g. Pratap et al. 1992; Keto et al. 2008; Sandell et al. 2009; Beuther et al. 2012, 2013), so that estimates of dust column density will be biassed. We note that C^{18}O is detected toward IRS1 and all the identified substructures of NGC 7358 S, even though its large-scale emission has been filtered out. As a rare isotopologue it is reasonable to assume its line is optically thin. We therefore use C^{18}O to make a second, independent estimate of the H_2 column density in these substructures. Assuming a constant abundance with respect to H_2, $x(C^{18}O) \approx 1.64 \times 10^{-7}$ (Wilson & Rood 1994; Giannetti et al. 2014), we can calculate the H_2 column density, reported in the column $N_{H_{2,2}}$ of Table 1. This is further discussed in Appendix C.3.

5.3. Molecular abundances

To study chemical properties, we derive the molecular abundances with respect to H_2 in each substructure with results shown in Tables A4–A6. In MM1–MM3, the H_2 column densities were derived from the 1.37 mm dust continuum emission, while for JetN and JetS where we did not detect dust continuum emission, we estimate the H_2 column density based on the integrated C^{18}O intensity ($N_{H_{2,2}}$). We argue that we are not strongly biassed, provided that the C^{18}O abundance is close to the canonical value in the ISM in MM1 (HMC), where the outflow emanated from (Wilson & Rood 1994). Since IRS1 and MM1 are both considered HMCs, we assume that their C^{18}O abundances are equal and therefore adopt $N_{H_{2,2}}$ when deriving the molecular abundance of IRS1.

6. 1-D model fit

Despite having similar H_2 column densities, adjacent condensations MM1–MM3 embedded in NGC 7538 S within 20,000 AU area, display gas temperature and spectral line properties which evolve systematically from the northeast to the southwest. We hypothesize that chemically MM1 evolves quickest, resulting in

[10] When T_{dust} > 100 K, water ice starts to sublimate. However, along the line of sight, temperature profiles at different radii of the protostar envelope are unknown. Therefore, we assume the dust absorption coefficient according to the thin ice mantle case, based on the modelling result in Gerner et al. (2014). In the most extreme case, if the ice is completely sublimated in MM1 or if MM3 still have larger water ice mantle, our current estimation leads to 2–4 times overestimation/underestimation of the H_2 column density.

[11] Table 1 shows that the projected sizes of MM1–MM3 from 2-D Gaussian fits are larger than the synthetic beam, so filling factors can be as one. Thus the number densities of MM1–MM3 are > 10^8 cm^{-3}.

[12] Jet/outflow-induced shocks may not only strip the ices mantles, but also partly destroy the grains.

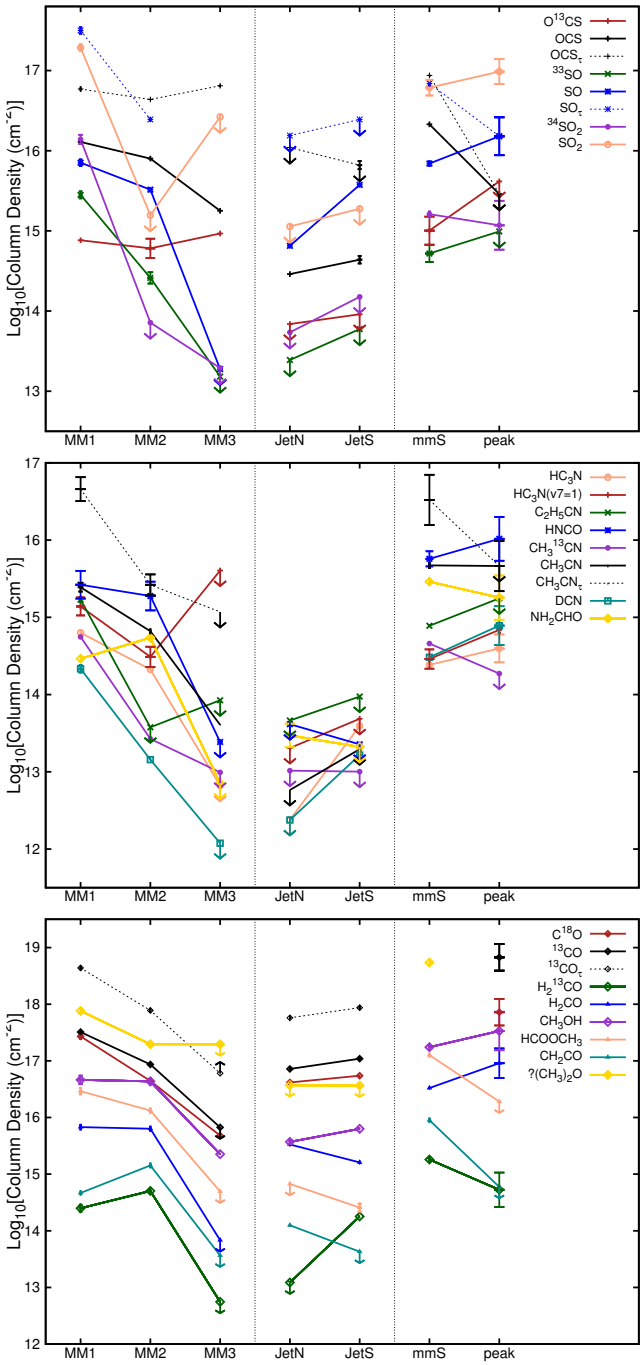

Fig. 5: Molecular column densities toward 5 positions in NGC 7538 S and 2 positions in IRS1. Colored solid lines show the variation for each isotopologue calculated with the optically thin assumption (arrows highlight the upper and lower limits), while dashed lines (OCS_τ, SO_τ, CH_3CN_τ, $^{12}CO_\tau$) show the variation calculated with opacity correction from Eq. B.10. The uncertainties at each position are determined from T_{rot}, partition function $Q(T_{rot})$, Gaussian fit to $\int T_B(\upsilon)d\upsilon$, or the scatter of the multi-transitions on the rotation diagrames (CH_3CN and HNCO). For species (e.g. HNCO, SO_2) we have not measured the optical depths, the column densities could be underestimated by a factor of 5-10.

the largest abundance of COMs, consistent with a HMC phase. Non-detection of most species in MM3 indicates that it remains in an early evolutionary stage (e.g. a prestellar object). Clear detections of COMs but generally lower gas temperatures and molecular abundances than in MM1 indicating that MM2 is at an intermediate evolutionary stage between MM1 and MM3. To verify our hypothesis, we iteratively fit the observed molecular column densities using the 'MUSCLE' ('MUlti Stage CLoud codE') 1-D chemical model (Semenov et al. 2010). This procedure has previously been successfully applied to fit the rich molecular data from several tens of HMSFRs at various evolutionary stages (Gerner et al. 2014), however at lower spatial resolution.

6.1. Physical model

In a 1-D approximation, we assume each condensation is well described by a spherically symmetric gas condensation, with a fixed outer radius of $r_{\rm out}$ = 1,100 AU (equal to the size of the PdBI synthesized beam), and are embedded in a large-scale, low-density envelope which shields the condensation from the interstellar FUV radiation with a visual extinction of 10 mag. In addition, we define a parameter $r_{\rm in}$ as the inner radius, within which temperature and density are assumed to be constants. The radial density and temperature profiles are therefore described by broken power laws,

$$\rho(r) = \begin{cases} \rho_{\rm in}(r/r_{\rm in})^{-p} & (r_{\rm out} \geq r \geq r_{\rm in}), \\ \rho_{\rm in} & (0 \leq r < r_{\rm in}) \end{cases} \quad (3)$$

and

$$T(r) = \begin{cases} T_{\rm in}(r/r_{\rm in})^{-q} & (r_{\rm out} \geq r \geq r_{\rm in}), \\ T_{\rm in} & (0 \leq r < r_{\rm in}) \end{cases} \quad (4)$$

Here, p and q are the radial indices of the density and temperature profiles, respectively. The gas and dust temperatures are assumed to be coupled.

In fitting each condensation model (Table. 3), we adjust the parameters p, $\rho_{\rm in}$, $T_{\rm in}$ and $r_{\rm in}$, keeping q fixed and equal to 0.4 (because of a highly optically thick medium, van der Tak et al. 2000). To derive the H_2 column density in the modelled large-scale cloud, we adopt a grid of 40 radial cells and integrate Eq. 3 numerically. We note that here the physical structure is assumed static (i.e. not evolving with time) for each condensation and is fitted iteratively to the observed chemical composition.

6.2. Chemical model

We use the time-dependent gas-grain chemical model 'ALCHEMIC' which is described extensively in Semenov et al. (2010) and Albertsson et al. (2013). The model is briefly summarized as follows.

(1) The chemical network is based on the OSU'2007 network[13], and is updated by implementing the most recent reaction rates (e.g. from the KIDA database[14], Albertsson et al. 2013).
(2) Both gas-phase and gas-grain interactions are included, resulting in 7907 reactions between 656 species made of 13 elements. The synthesis of COMs was included using a set of surface reactions (together with desorption energies) and photodissociation reactions of ices (Garrod & Herbst 2006; Semenov & Wiebe 2011).
(3) Cosmic-ray particles (CRP, $\zeta_{\rm CR} = 5 \times 10^{-17}$ s^{-1}) and CRP-induced FUV radiation are considered to be the only external ionizing sources. For these we adopt the UV dissociation and ionization photo-rates from van Dishoeck et al. (2006), assuming the case corresponding to the spectral shape of the interstellar FUV radiation field.
(4) Sticking : Molecules, other than H_2 which has a binding energy of $\sim$ 100 K (Lee 1972), are assumed to stick to grain surfaces with 100% probability.
(5) Mobility: On the surface sites quantum tunnelling is not considered (Katz et al. 1999).
(6) Reactions: Dissociative recombination is modelled, resulting in the ion-ion neutralization and electron attachment on the grains, while chemisorption of surface molecules is not considered. Each 0.1 μm spherical olivine grain provides $\approx 1.88 \times 10^6$ surface sites for accreting gaseous species and the surface recombination proceeds solely through the Langmuir-Hinshelwood formation mechanism.
(7) Release: As the temperature increases, ices are released back to the gas phase by thermal, CRP, and CRP-induced UV-photodesorption (UV yield is 3×10^{-3}, e.g. Öberg et al. 2009). In addition, all freshly formed surface molecules are assumed to have a 1% chance to leave the grain surface upon recombination.
(8) None of the above chemical parameters were varied during the iterative fitting of the observational data.

[13] http://www.physics.ohio-state.edu/ eric/research.html
[14] http://kida.obs.u-bordeaux1.fr

6.3. modelling scheme

Given the very close location of the condensations MM1–MM3 to each other, it is natural to assume that they fragmented from a common parental core, as soon as the gas core became cold and dense enough. The IRDC-like physical conditions seem to be the most appropriate for that. Thus we assume that the condensations MM1–MM3 evolved both physically and chemically from the same parental IRDC.

This allows us to set up the initial chemical abundances for our modelling. Following the multi-stage MUSCLE scheme in Gerner et al. (2014), we took a single-point (0-D) IRDC physical model with the best-fit parameters by fitting the median of their observed IRDC sample. The 0-D assumption merely reflects our lack of knowledge about the real structure of the MM progenitor core.

Therefore, the pre-MM IRDC is reasonably assumed to have a single temperature of 15 K, a hydrogen particle density of 2×10^5 cm^{-3} and a chemical age of 11,000 years. Note when we model the chemical composition with such a simplistic physical structure, the "chemical age" is the physical time moment when our chemical code describes the observed column densities most accurately.

With this 0-D IRDC physical model, we use our gas-grain ALCHEMIC code to compute its chemical evolution over the chemical age of 11,000 years, starting from the "low metals" initial abundances of Lee et al. (1998) (see also Table 2). The resulting abundances are used as input to subsequent chemical modelling of later evolutionary stages.

After 11,000 years of the IRDC evolution, we assume it fragmented into three individual MM condensations, which underwent gravitational collapse at various speeds, due to for example, difference in initial masses or angular momenta. Using observed temperatures of the condensations MM1–MM3 as a rough estimate of how much they have evolved physically, it becomes clear that MM3 with T $\sim$ 50 K is younger (less evolved) than MM2 with T $\sim$ 137 K, which is in turn younger than MM1 with T $\sim$ 172 K (see Table 1). This also means that MM1 has likely passed through physical conditions which were similar first to MM3 and then to MM2 phase, while MM2 has passed only through MM3-like evolutionary phase. As we do not know exactly how density and temperature of each MM

Table 2: Top 35 initial abundances for the parental IRDC 0-D model at 11,000 years.

Species	Relative abundance	Species	Relative abundance
H_2	5.00(−01)	H	9.75(−02)
He	3.77(−04)	C	1.79(−05)
CO	2.35(−05)	N	1.24(−05)
O	8.16(−05)	CH_4 ice	2.63(−05)
H_2O ice	6.79(−05)	NH_3 ice	1.02(−05)
C_3	1.17(−06)	CH_3OH ice	5.39(−06)
CH_4	4.07(−07)	H_2O	9.43(−07)
N_2	7.75(−07)	C_3H_4 ice	3.27(−07)
CO_2 ice	1.43(−07)	N_2 ice	1.62(−07)
CH_2CO	1.43(−08)	CH_2OH	2.11(−08)
CH_3OH	1.35(−08)	CN	1.04(−08)
CO_2	1.85(−08)	e^-	1.96(−08)
HCN	2.41(−08)	HNC	2.36(−08)
NH_3	2.54(−08)	O_2	1.63(−08)
OH	1.16(−08)	S	8.29(−08)
CO ice	1.71(−08)	H_2CO ice	1.77(−08)
HCN ice	1.22(−08)	C^+	1.77(−09)
C_2H	2.05(−09)		

condensation evolved, we assume a jump-like transition[15] of the physical properties from phase to phase. This is a crude approximation of more smoother, gradual increase in density and temperature during the collapse, but it enables us to apply our multi-stage chemical modelling approach.

For that, the IRDC chemical composition at $t = 11,000$ years was taken as the input to the 1-D power-law physical model described in Sec. 6.1 and the observed column densities of the MM3 condensation were iteratively fitted. Then, we used the best-fit MM3 chemical structure as an input for similar iterative 1-D chemical fitting of the more evolved MM2 condensation. After that, we repeated the same procedure and used the best-fit MM2 chemical structure as an input to model and to fit the observed column densities in the MM1 condensation.

6.4. Iterative fit to the data

The best-fit result of the models described above was obtained via an iterative procedure. Parameters, including the inner radius $r_{\rm in}$, the density at the inner radius $\rho_{\rm in}$, the temperature at the inner radius $T_{\rm in}$ and the density slope p, were adjusted to the following constraints:

1. The density index p is restricted to 1.0–2.5 (Guertler et al. 1991; Beuther et al. 2002; Mueller et al. 2002; Hatchell & van der Tak 2003).
2. The derived H_2 column densities set $r_{\rm in}$ (1–300 AU) and $\rho_{\rm in}$ ($10^{10} - 10^{13}$ cm^{-3}) within a factor of 3.
3. Based on our previous temperature estimates (Section 5.1), $T_{\rm in}$ is limited to $30 - 80$ K for MM3 and to $100 - 300$ K for the MM2 and MM1 condensations, respectively.

By varying the above parameters and fixing the rest, a model grid for each condensation consisting of 1,000–3,000 parameter combinations was produced.

We modelled the physical and chemical structures of MM1–MM3 over a period of 10^5 years (over 99 logarithmic time steps), and compared the modelled beam-averaged molecular column densities with the observed values. The goodness-of-fit, measured by χ^2, for each model at each time step was estimated using a confidence criterion taken from Eq. (3) in Garrod et al. (2007), where the standard deviation for each detected species is taken as ~ 0.3 dex. For species where our observations only provided upper limits for their column densities, we manually set the goodness-of-fit to be 0 once the modelled column density is more than 10 times lower than the observed upper limit. Subsequently, a total goodness-of-fit was obtained as the mean value of the confidence criteria for all species at a given time step and with a given parameter combination. Minimizing χ^2-value yielded the best-fit physical model and the best-fit chemical age for our observations.

Our best fit parameters for the three observed condensations are listed in Table. 4. Molecular abundances with respect to H_2 are shown in Figure 6, with the black lines representing observed values and the red filled area representing the modelling range. The x-axis shows the chemical variations from MM1 to MM3. From the above fitting, we found that the time for a pre-MM3 object to chemically evolve to a MM1-like object is short[16] (10–450 yrs), indicating that the fast chemical evolution in the process from MM3-like structure to MM1-like structure leads to significant chemical differences.

7. Discussion

This is the first comprehensive comparison of molecular lines observed at high spatial resolution with chemical models towards the NGC 7538 S and IRS1 regions. By resolving substructures we have unveiled chemical variation on a ∼1,100 AU scale between gas condensations which originate from the same natal gas cores. In the following section we discuss our findings.

7.1. Comparison with other results

7.1.1. Relation to the large-scale HMSFR studies

The derived gas column densities of the condensations (MM1–MM3) are comparable across all three condensations, $(1–5) \times 10^{24}$ cm^{-2}, and are also consistent with the derivations from the previous observations and simulations (e.g. Naranjo-Romero et al. 2012).

In addition, we have observed 7 species ($C^{18}O$, H_2CO, CH_3OH, OCS, SO, HNCO, and CH_3CN) which were previously observed in a survey of HMSFRs covering a broad range of evolutionary stages (Gerner et al. 2014). Due to the relatively coarse spatial resolution of the larger survey (10^5 AU), their observed chemical properties are potentially biassed towards the embedded, chemically most evolved gas substructures. For

[15] A temperature change occurs when simulations from one phase go to another phase: T(r) is kept constant with time during each evolutionary phase and is replaced by a new (warmer) temperature profile at each phase end.

[16] Such short best-fit chemical ages are caused by very high densities of $\gtrsim 10^{10}$ cm^{-3} and warm temperatures $\gtrsim 50$ K in the best-fit models. Under these specific conditions, chemical evolution is driven by very rapid gas-phase processes, which are able to quickly "reset" the initial chemical composition from a cold IRDC phase. More precisely, it is a steep, jump-like transition from the progenitor IRDC phase with a density of $\sim 10^5$ cm^{-3} to the MM3 phase with a density of $> 10^{10}$ cm^{-3} that makes the resulting best-fit chemical ages so short.

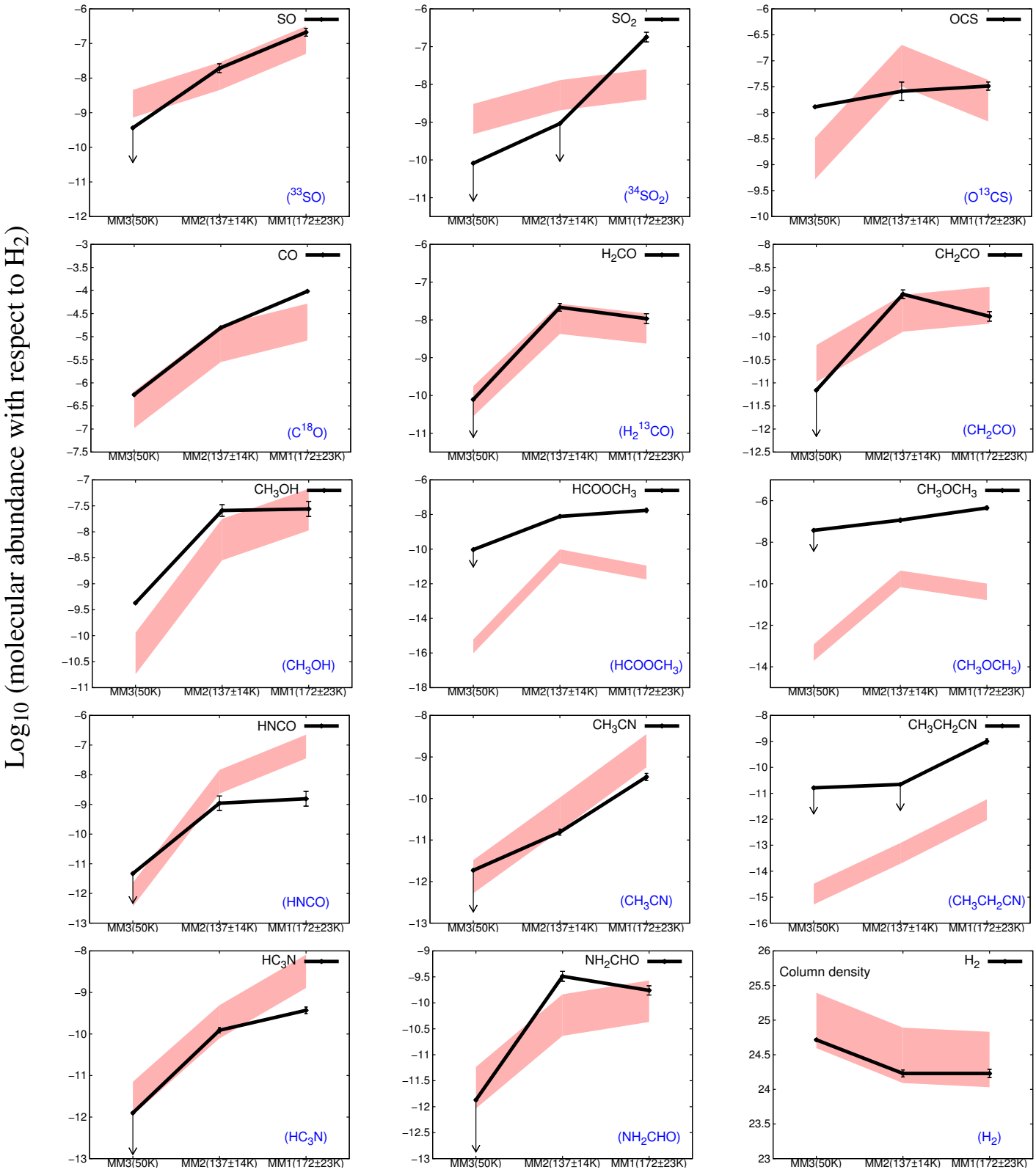

Fig. 6: Best fit of molecular abundances in MM1–MM3, with the chemical ages of 11200 yrs, 11210 yrs, and 11660 yrs, respectively. The last panel shows the best fit of H_2 column density, whose observed values are derived from dust emission. The modelled values and tolerance (0.1–10) are shown as a red filled region, while the observed values are plotted as solid black lines, with the uncertainties determined from T_{rot}, partition function $Q(T_{rot})$, and Gaussian fit to $\int T_B(\upsilon)d\upsilon$ or scatter of transitions (CH_3CN and HNCO). Abundances of species (name in black at the upper-right corner of each panel) are derived from their detected rare isotopologues, or opacity correction, or from optically thin assumption, which are all named in blue in parentheses at the lower-right corner of each panel.

Table 3: Parameters of the best-fit 1-D gas-grain condensation models of MM1–MM3

I. Parameters of the best-fit condensation models.

Parameter	Symbol	MM3[a]	MM2[a]	MM1[a]
Inner radius	$r_{\rm in}$	3.7 AU	1.1 AU	1.1 AU
Outer radius[b]	$r_{\rm out}$	1100 AU	1100 AU	1100 AU
Density within the inner radius	$\rho_{\rm in}$	1.01×10^{13} cm^{-3}	1.1×10^{11} cm^{-3}	6.1×10^{12} cm^{-3}
Density beyond the outer radius	$\rho_{\rm out}$	1.2×10^{8} cm^{-3}	1.1×10^{8} cm^{-3}	4.8×10^{7} cm^{-3}
Density profile	p	2.0	1.0	1.7
Beam-averaged density	$\bar{\rho}$	4.7×10^{9} cm^{-3}	4.1×10^{8} cm^{-3}	8.7×10^{8} cm^{-3}
Temperature within the inner radius	$T_{\rm in}$	59.4 K	229.2 K	278.6 K
Temperature beyond the outer radius	$T_{\rm out}$	10.0 K	14.5 K	17.6 K
Temperature profile	q	0.4	0.4	0.4
Beam-averaged temperature	$\bar{T}$	14.1 K	20.6 K	28.5 K
Mass	M	2.5 $M_\odot$	3.8 $M_\odot$	8.3 $M_\odot$

Note. *a*. The values listed were obtained at the end of each evolutionary stage, corresponding to the values used in Figure 6.
b. This value is limited by the 0.4″ PdBI synthesized beam size used in our observations.

Table 4: Best-fit 1-D gas-grain modelled column densities compared to the observed values in MM1–MM3

Molecule[d,e]	MM3[f]		MM2[f]		MM1[f]		Notes on the Observed Values
	$N^g_{\rm Observed}$ (cm^{-2})	$N^h_{\rm Modeled}$ (cm^{-2})	$N^g_{\rm Observed}$ (cm^{-2})	$N^h_{\rm Modeled}$ (cm^{-2})	$N^g_{\rm Observed}$ (cm^{-2})	$N^h_{\rm Modeled}$ (cm^{-2})	
H_2	$5.25_{\pm0.23}(24)$	9.9(24)	$1.70_{\pm0.22}(24)$	3.1(24)	$1.69_{\pm0.27}(24)$	2.7(24)	derived from dust continuum
CO	$2.39_{\pm0.06}(18)$	2.6(18)	$2.21_{\pm0.16}(19)$	2.2(19)	$1.35_{\pm0.16}(20)$	5.6(19)	derived from $C^{18}O$ with $^{16}O/^{18}O = 607^a$
H_2CO	$\leq 4.95(14)$	7.0(14)	$4.50_{\pm0.51}(16)$	3.3(16)	$2.22_{\pm0.34}(16)$	1.6(16)	derived from $H_2^{13}CO$ with $^{12}C/^{13}C = 73^a$
CH_2CO †	$\leq 3.67(13)$	2.6(14)	$1.43_{\pm0.12}(15)$	1.0(15)	$4.66_{\pm0.37}(14)$	1.3(15)	
CH_3OH †	$2.25_{\pm0.02}(15)$	4.5(14)	$4.33_{\pm0.58}(16)$	2.2(16)	$4.61_{\pm0.88}(16)$	7.2(16)	
$HCOOCH_3$ †	$\leq 4.95(14)$	2.4(09) ×	$1.33_{\pm0.13}(16)$	1.2(14) ×	$2.91_{\pm0.39}(16)$	1.2(13) ×	
CH_3OCH_3 *†	$\leq 1.96(17)$	4.8(11) ×	$1.97_{\pm0.19}(17)$	5.3(14) ×	$7.62_{\pm0.57}(17)$	1.1(14) ×	
HNCO †	$\leq 2.44(13)$	9.1(12)	1.89±1.01(15)	1.8(16)	2.64±1.35(15)	2.4(17) ×	
HC_3N †	$\leq 6.60(12)$	2.8(13)	$2.11_{\pm0.03}(14)$	6.1(14)	$6.33_{\pm0.12}(14)$	8.7(15) ×	
CH_3CN	$\leq 1.18(15)$	1.3(13) ×	2.64±0.96(15)	1.3(14) ×	4.58±1.97(16)	3.8(15)	derived from opacity corrected CH_3CN in Sec. 5.2.1
CH_3CH_2CN †	$\leq 8.43(13)$	1.3(10) ×	$\leq 3.77(13)$	1.5(11) ×	$1.70_{\pm0.13}(15)$	6.3(12) ×	
NH_2CHO †	$\leq 7.11(12)$	2.3(13)	$5.46_{\pm0.50}(14)$	1.8(14)	$2.91_{\pm0.13}(14)$	2.9(14)	
OCS	$8.25_{\pm0.11}(16)$	1.3(16)	$5.39_{\pm1.71}(16)$	2.5(17)	$6.79_{\pm0.14}(16)$	4.6(16)	derived from $O^{13}CS$ with $^{12}C/^{13}C = 73^a$
SO_2	$\leq 4.29(14)$	1.2(16) ×	$\leq 1.58(15)$	1.6(16)	$3.05_{\pm0.43}(17)$	2.7(16) ×	derived from $^{34}SO_2$ with $^{32}S/^{34}S = 22^b$
SO	$\leq 1.93(15)$	1.8(16)	$3.29_{\pm0.58}(16)$	3.5(16)	$3.57_{\pm0.38}(17)$	3.4(17)	derived from ^{33}SO with $^{32}S/^{33}S = 127^b$
Agreement		10/15 = 67%		11/15 = 73%		9/15 = 60%	
Age [c]		11200 yrs		11210 yrs		11660 yrs	

Note. *a*. derived from galactic local isotope ratio (Giannetti et al. 2014);
b. derived from isotope ratio in solar system (Lodders 2003);
c. The physical time moment when our chemical code describes the observed column densities most accurately in our assumed physical structures.
d. "*" denotes the tentatively identified line;
e. "†" denote the species which do not have rare isotopologues, so we derive their values by assuming they are optically thin;
f. "×" denote the model predicted column densities inconsistent to the observation ($N_{\rm Modeled}/N_{\rm Observed} < 0.1$ or > 10);
g. Uncertainties of the observed value are determined from $T_{\rm rot}$, partition function $Q(T_{\rm rot})$, and Gaussian fit to $\int T_B(\upsilon)d\upsilon$;
h. The values listed were obtained at the end of each evolutionary stage, corresponding to the values used in Figure 6.

example, the averaged chemical and spectral line properties of the entire NGC 7538 S region, appear very similar to those of the condensation MM1 (a HMC).

Our results suggest that abundances of these species on the small scales of MM1, MM2, and MM3 all approximately agree with the abundances measured in large-scale HMCs, HMPOs, and prestellar objects, respectively. This not only supports our hypothesis that MM3 is the youngest condensation, but also reinforces the idea of an evolutionary sequence from southwest (least evolved) to northeast (most evolved).

7.1.2. Evolutionary stage of IRS1

In contrast to the resolved fragments in NGC 7538 S, IRS1 remains an unresolved compact core at 1.37 mm, which has a much higher intensities of both continuum and lines than in NGC 7538 S. Based on the H_2 column density we estimated from $C^{18}O$, we expect that the dust thermal continuum emission contributes to ~ 0.07 Jy beam^{-1} at the peak of the 1.37 mm continuum image, roughly 3.6% of the peak continuum intensity, free-free emission may contribute to 96.4% of the total flux (of 3.38 Jy), which is ~ 3.25 Jy.

We estimated the CH_3CN rotational temperature from the off-peak position IRS1-mmS, taken this as the lower limit, and assumed the temperature from Goddi et al. (2015) at higher resolution as the upper limit of IRS1-peak temperature. This gas temperature range is consistent with that in Knez et al. (2009); Qiu et al. (2011); Zhu et al. (2013). Moreover, the lower limit column densities of HNCO, ^{13}CO, and CH_3CN agree with the aforementioned study. Furthermore, the CH_3CN abundance at the IRS1-peak (~ 10^{-10}) also agree with what are typically

observed from HMCs (Hatchell et al. 1998; Chen et al. 2006; Zhang et al. 2007).

As we have detected more COM lines in IRS1-mmS than in MM1 (Table A1) and found that IRS1 has the highest luminosity in the NGC 7538 region (Scoville et al. 1986), we consider IRS1 to be chemically and dynamically more evolved than MM1. This is in line with the notion that at larger scales the evolutionary sequence proceeds from the southeast ("youngest") to northwest ("oldest") (McCaughrean et al. 1991).

7.2. Hierarchical fragmentation in NGC 7538 S: synthesis of observations and models

The giant molecular cloud NGC 7538 fragments into at least three bright gas cores, namely IRS1, IRS9, and NGC 7538 S. The large-scale gas core NGC 7538 S continues to fragment, agreeing with the picture of "hierarchical fragmentation". The separations of the three spatially resolved internal condensations in NGC 7538 S, are on the order of 3,800-5,000 AU. Given that these condensations are in the same gas core and have similar projected sizes and column densities, they are likely to have similar dynamic ages. The significant variation in molecular line intensities and abundances among them indicate an evolutionary sequence from MM3 through MM2 to MM1.

7.2.1. MM1–MM3 evolutionary stages

MM1 is characterized as a typical HMC owing to its high temperature (> 150 K), high optical depth and high abundance of COMs. In fact, its presence of bright IR emission suggests that this condensation is at a chemically more evolved stage in chemical terms compared to many other HMCs (e.g. Chen et al. 2006; Zhang et al. 2007; Girart et al. 2009; Qiu & Zhang 2009). Previous VLA observations (Wright et al. 2012) towards MM2 and MM3 did not detect radio continuum sources, suggesting that they are in early protostellar phases. We observed that some species in MM2 exhibit less intensity of emission than in MM1 (e.g. H_2CO, CH_3OH, $HCOOCH_3$, OCS), while some species exhibit the strongest emission in MM2, but they are barely detected in MM3 (e.g. $H_2^{13}CO$, CH_2CO, NH_2CHO, which are evaporated to gas at ~ 40 K and may further interact with other radicals at higher temperature to produce the more complex molecules, see Figure 8(d) of Garrod et al. 2008). This suggests that MM2 should be chemically more evolved than MM3. As a result, we assert MM2 could be in the HMPO stage while MM3 is potentially still a prestellar object. While the temperatures of MM3 around 50 K are too high for a genuine isolated prestellar object, in the cases of the two neighboring more evolved cores, the elevated temperatures in MM3 may also be caused by radiation interactions of these neighbors.

7.2.2. Warm-up histories

We adopt the terminology of "chemical warm-up timescale" from Garrod et al. (2008). This timescale in our model refers to the period over which the temperature within the inner radius r_{in} of a source increases from an initial value (e.g. 10-20 K) to a higher value (e.g. > 100 K)[17]. We found temperature rises steeply and not linearly with time in our model. We derive a general picture of hierarchical fragmentation in NGC 7538 S.

While we are unable to distinguish whether MM1–MM3 are originated from a massive and unstable rotating gas torus, or are formed via fragmentation of a dusty core (Corder 2009; Wright et al. 2012; Naranjo-Romero et al. 2012), both scenarios will lead to a similar "dynamic age" (i.e. collapsing simultaneously) of these condensations, and therefore do not change our interpretation of chemical evolution. As our model shows, differences in the chemical age of these condensations are small: $\sim 10 - 10^2$ years. Such slight variations in timescale may be caused by the different physical environments (Ballesteros-Paredes et al. 2007), e.g. turbulence, gravitational potential, magnetic fields, etc., which can cause different evolution speeds. In our picture, MM1 warms up faster than MM2 and MM3. At a particular physical age ($\sim 10^4$ years), when the abundances of H_2CO, CH_2CO, and NH_2CHO reach their maximum in MM2, their abundances already begin to decrease in MM1 because they are reacting to form the more complex, second-generation molecules, while MM3 is still in chemically the least evolved phase and most of the molecules are still on the grain surfaces due to its slowest speed.

7.3. The absorption and emission feature in IRS1

7.3.1. General P-Cygni and absorption profiles

Most of the observed molecular lines at 1.37 mm display P-Cygni or inverse P-Cygni /pure absorption features against the bright continuum source IRS1 within a 0.4″area. In previous kinematics studies the P-Cygni feature was interpreted as associating with jet(s)/outflow(s) from a disk-like structure, while the inverse P-Cygni and pure absorption features were interpreted by rotation and infalling gas (Wilson et al. 1983; Henkel et al. 1984; Sandell et al. 2009; Qiu et al. 2011; Beuther et al. 2012, 2013; Zhu et al. 2013). However, whether the protostellar disk is face-on (Kawabe et al. 1992; Beuther et al. 2013) or edge-on (e.g. Pestalozzi et al. 2004; Lugo et al. 2004; De Buizer & Minier 2005; Knez et al. 2009), whether the direction of the associated outflow is perpendicular (e.g. De Buizer & Minier 2005; Knez et al. 2009; Zhu et al. 2013) or along (e.g. Beuther et al. 2013) our line of sight or precessing (e.g. Kraus et al. 2006), and whether the IRS1-peak is a single protostar or binary system (Moscadelli et al. 2009; Moscadelli & Goddi 2014; Goddi et al. 2015) are still under debate.

7.3.2. Pure emission lines tentatively from CH_3OH and $HCOOCH_3$

At least four bright molecular lines do not show absorption toward the IRS1-peak (marked with "?" in Figure 2). Since these lines are also detected from MM1 and IRS1-mmS, we fit them by the synthetic spectrum programme and map their spatial distribution in NGC 7538 S (Figure 7) and IRS1 (Figure 8). We propose that three of them (at 217.299 GHz, 217.643 GHz, and 217.886 GHz, Table 5) are CH_3OH transitions with FWHM$\sim$ 2.5 km s^{-1}. This is supported by the emission of another CH_3OH transition at the IRS1-peak (at 356.007 GHz,

[17] In fact, the entire process is more complicated than just the increase of temperature. When a prestellar object is forming, it may initially be warmer, ~20 K, and then it cools off as it becomes more dense to T ~10 K (in the center). When collapse begins, T rises from 10 K to several hundreds K.

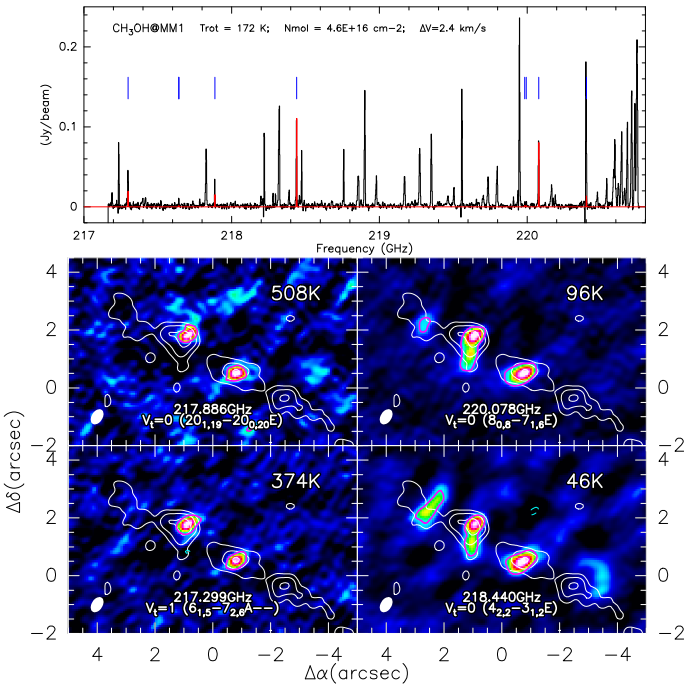

Fig. 7: The upper panel shows a synthetic spectrum of CH_3OH fitted to the MM1 data. The black histogram is the observed spectrum, overlaid with the red fit whose parameters are listed. Blue lines mark transition frequencies, and confirm that lines at 217.299 GHz, 217.643 GHz, 217.886 GHz are CH_3OH. The lower panel presents intensity integrated maps over the velocity range from -65 to -50 km s^{-1} ($V_{lsr} \sim -60$ km s^{-1} in MM1), with red contours showing the 3σ rms. White contours show the continuum (at 4σ, 14σ, and 24σ levels).

Table 5: Parameters of detected CH_3OH lines from CDMS

ν (MHz)	Transition	E_u/k (K)	
217299	$\nu_t = 1(6_{1,5} \rightarrow 7_{2,6}A--)$	374	emission
217643	$\nu_t = 1(15_{6,9} \rightarrow 16_{5,12}A++)$	746	emission
	$\nu_t = 1(15_{6,10} \rightarrow 16_{5,11}A--)$		
217886	$\nu_t = 0(20_{1,19} \rightarrow 20_{0,20}E)$	508	emission
218440	$\nu_t = 0(4_{2,2} \rightarrow 3_{1,2}E)$	46	absorption
220079	$\nu_t = 0(8_{0,8} \rightarrow 7_{1,6}E)$	96	absorption
356007*	$\nu_t = 0(15_{1,14} \rightarrow 15_{0,15}A++)$	295	emission

"*" from Beuther et al. (2013)

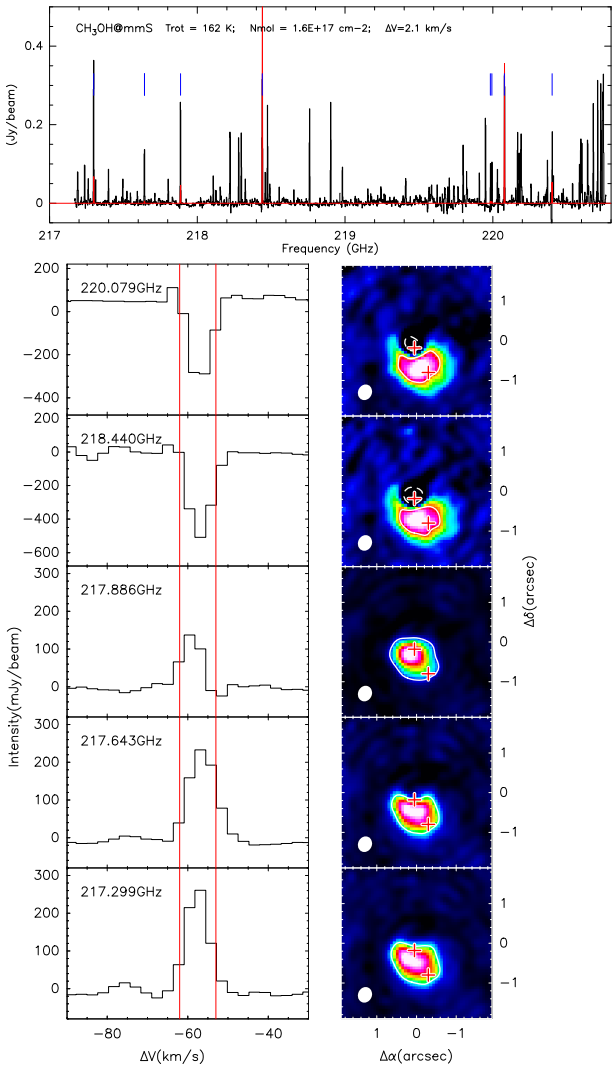

Fig. 8: The upper panel shows the fitted CH_3OH spectrum in IRS1-mmS. The black histogram is the observed spectrum, overlaid with the red fit whose parameters are listed. Blue lines mark transition frequencies at 217.299 GHz, 217.643 GHz, 217.886 GHz. The lower left panel shows the line profiles of CH_3OH transitions from the IRS1-peak; and the right panel presents corresponding intensity maps integrated over the velocity range from -63 to -53 km s^{-1} ($V_{lsr} \sim -58$ km s^{-1} at the continuum peak). The red crosses mark the IRS1-peak position and IRS1-mmS, and the yellow solid (dashed) contour shows ±4σ rms level.

Beuther et al. 2013). We note that these four CH_3OH lines have upper state energy levels $E_u/k > 250$ K, while the other two absorption E-type CH_3OH lines have $E_u/k < 100$ K.

Moreover, we also note that some $HCOOCH_3$ transitions also show tentatively ($\sim 3\sigma$ rms) pure emission toward the IRS1-peak (denoted in Table. A1 and shown in Figure A1). Compared to the CH_3OH lines, the emission of $HCOOCH_3$ lines are weaker. Eight out of ten reliable pure emission $HCOOCH_3$ lines are torsionally excited ($\nu_t = 1$) with $E_u/k > 250$ K. It is likely that they have the same origin as the pure emission CH_3OH transitions.

7.3.3. Proposed explanations for the emission lines at IRS1-peak

One hypothesis for the simultaneous absorption and emission is that the outflow penetrates the envelope, producing a collimated, jet-like cavity along the line of sight. Here, transitions with higher E_u/k from the inner hot core are detected in emission; the other lines of CH_3OH with lower E_u/k are produced outside of the cavity, and are absorbed by the colder envelope. Our observations with limited spectral resolution did not reveal a velocity offset, higher angular resolution cm observations ($\sim$ 200 AU) have resolved the IRS1-peak into two components, showing $\sim$ 3 km s^{-1} CH_3OH maser radial velocity offset

(Moscadelli et al. 2009; Goddi et al. 2015). As a result, different structural components might explain the co-existence of the absorption and pure emission line features.

Moreover, we note from Figure 8 that the line at 217.886 GHz is the only CH_3OH line that emits and peaks unambiguously at the IRS1-peak, and that the other two emission lines seem $\sim 0.5''$ offset southern to IRS1-peak. Therefore, a second hypothesis may be that the CH_3OH absorption is due to a colder environment, while IRS1-mmS might be the foreground relative to the UCHII.

In addition to the possible effects of the source geometry or different origins of multi-transitions, a third possibility to explain the pure emission lines are non-LTE effects or masering. The strong and compact continuum radiation of IRS1 can excite most molecular lines with lower E_u/k, pumping them to higher rotational levels. CH_3OH masers are traditionally classified into two groups (Menten 1991): collisionally pumped (Cragg et al. 1992) Class I and radiatively pumped Class II (Sobolev et al. 2007 and references therein, Cragg et al. 2005). Class I masers trace shocks from molecular outflows and jets during the earliest stages of star formation (Plambeck & Menten 1990; Voronkov et al. 2006; Sutton et al. 2004). Class II masers are typically associated with hyper-compact HII regions (e.g. Minier et al. 2001; Ellingsen 2006), where strong free-free emission can dominate the dust emission up to frequencies as high as 300 GHz (Kurtz 2005; Sobolev et al. 2007). Although there are no other observations confirming which class of masers our observed CH_3OH emission lines may be, cm large-scale (FWHP $\sim 43''$) observations of IRS1 suggest that a different torsionally excited CH_3OH emission line ($9_2 \rightarrow 10_1$A+) a probable Class II maser (Wilson et al. 1984), and another torsionally excited CH_3OH absorption line ($10_1 \rightarrow 11_2$A+) is not in LTE (Menten et al. 1986). Therefore, "quasi-masing"[18] may induce the emission from torsionally excited CH_3OH.

8. Conclusion

We have performed high angular resolution observations of the two high-mass star-forming gas cores NGC 7538 S and IRS1. These observations were complemented with a suite of chemical models with the aim of disentangling the chemical evolution of the individual sources. Our main conclusions are summarized as follows.

1. NGC 7538 S is one of the brightest gas fragments in the NGC 7538 molecular cloud. Our 1.37 mm observations with $\sim 1,100$ AU ($0.4''$) spatial resolution have resolved this region into at least three gas condensations. Each condensation exhibits similar continuum specific intensities, but significantly different chemical complexity. We covered over 90 molecular lines from 15 species, including 22 isotopologues; most showed emission peaks at MM1. A few ($H_2^{13}CO$, CH_2CO, and NH_2CHO) have higher intensity emission in MM2 and are relatively weak or undetected in MM3. Comparing our chemical study on small scales (10^3 AU) to the previous large sample statistics on large scales (10^5 AU), we found that the molecular abundances in MM1, MM2, and MM3 generally agree with the values measured in HMCs, HMPOs, and IRDCs (prestellar objects), respectively.
2. Comparing our observations with a 1-D gas-grain chemical model, we propose an evolutionary sequence along the northeast-southwest filamentary NGC 7538 S. MM1–MM3 may be fragments formed from a global collapse within $\sim$ 20,000 AU. However, the heating paces from their internal protostars /prestellar objects are likely different. Slight variations may be caused by mechanisms such as turbulence, gravitational potential, or magnetic fields. Our chemical model suggests that the protostar in MM1 ignited first, making it chemically the most evolved source. MM2 has an intermediate warm-up speed while the central object in MM3 may still be a prestellar object. Although the chemical histories of MM1–MM3 are not synchronized, the differences in their chemical ages are small (several hundred years), indicating that the chemical evolution of HMSFR is sensitive to the warm-up speed. Evolution from an MM3-like condensation to an MM1-like condensation can be rapid. Given our model limitations, evolution may take longer time, so precise dating of the central condensations of HMSFRs from their chemical compositions needs our better understanding of the internal structures of the sources.
3. Our chemical model successfully fits the chemical variations for > 60% of the observed species in MM1–MM3. However, abundances of COMs are poorly fit across the condensations. The intrinsically weak nature of these lines (especially in MM3), the limitations of the chemical network in dealing with more complex chemistries and the unknown complicated source structure (Appendix C) are likely causing these discrepancies. To improve the modelling process, further observations, e.g. using single-dish telescopes, are required to recover information on all scales, better description of the formation and excitation of COMs are needed in the chemical networks, and a more appropriate physical structure combined with dynamic processes have to be taken fully into account.
4. IRS1 is dynamically and chemically the most evolved core in the NGC 7538 clump. We detected primarily absorption lines, but also a few lines showing pure emission (e.g. CH_3OH and $HCOOCH_3$). These emission lines may be caused by unresolved sub-entities in IRS1-peak, or non-LTE (quasi-masing) effects of certain line transitions.

[18] A non-LTE status of the line with high E_u/k, which can be detected in much lower temperature environment (than E_u/k) because of certain pumping mechanism.

Acknowledgements. We would like to thank the IRAM staff for their support during the observation and data reduction process. We thank Karin Öberg, Hauyu Baobab Liu, and Malcolm Walmsley for useful discussions.
This research made use of NASAs Astrophysics Data System. S.F. acknowledges financial support by the European Community Seventh Framework Programme [FP7/2007-2013] under grant agreement no. 238258.
D.S. acknowledges support by the *Deutsche Forschungsgemeinschaft* through SPP 1385: "The first ten million years of the solar system - a planetary materials approach" (1962/1-3).

References

Akabane, K. & Kuno, N. 2005, A&A, 431, 183
Albertsson, T., Semenov, D. A., Vasyunin, A. I., Henning, T., & Herbst, E. 2013, ApJS, 207, 27
Andersson, M., Askne, J., & Hjalmarson, A. 1984, A&A, 136, 243
Ao, Y., Henkel, C., Menten, K. M., et al. 2013, A&A, 550, A135
Argon, A. L., Reid, M. J., & Menten, K. M. 2000, ApJS, 129, 159
Bachiller, R. & Pérez Gutiérrez, M. 1997, ApJ, 487, L93
Ballesteros-Paredes, J., Klessen, R. S., Mac Low, M.-M., & Vazquez-Semadeni, E. 2007, Protostars and Planets V, 63
Balog, Z., Kenyon, S. J., Lada, E. A., et al. 2004, AJ, 128, 2942

Barentine, J. C. & Lacy, J. H. 2012, ApJ, 757, 111
Beuther, H., Churchwell, E. B., McKee, C. F., & Tan, J. C. 2007, Protostars and Planets V, 165
Beuther, H., Linz, H., & Henning, T. 2012, A&A, 543, A88
Beuther, H., Linz, H., & Henning, T. 2013, A&A, 558, A81
Beuther, H., Schilke, P., Menten, K. M., et al. 2002, ApJ, 566, 945
Bisschop, S. E., Jørgensen, J. K., van Dishoeck, E. F., & de Wachter, E. B. M. 2007, A&A, 465, 913
Boucher, D., Burie, J., Bauer, A., Dubrulle, A., & Demaison, J. 1980, Journal of Physical and Chemical Reference Data, 9, 659
Campbell, B. 1984, ApJ, 282, L27
Campbell, B. & Thompson, R. I. 1984, ApJ, 279, 650
Chen, H.-R., Welch, W. J., Wilner, D. J., & Sutton, E. C. 2006, ApJ, 639, 975
Chin, Y.-N., Henkel, C., Whiteoak, J. B., Langer, N., & Churchwell, E. B. 1996, A&A, 305, 960
Churchwell, E., Wood, D., Myers, P. C., & Myers, R. V. 1986, ApJ, 305, 405
Clark, B. G. 1980, A&A, 89, 377
Corder, S. A. 2009, PhD thesis, California Institute of Technology
Cragg, D. M., Johns, K. P., Godfrey, P. D., & Brown, R. D. 1992, MNRAS, 259, 203
Cragg, D. M., Sobolev, A. M., & Godfrey, P. D. 2005, MNRAS, 360, 533
De Buizer, J. M. & Minier, V. 2005, ApJ, 628, L151
Draine, B. T. 2011, Physics of the Interstellar and Intergalactic Medium
Ellingsen, S. P. 2006, ApJ, 638, 241
Elmegreen, B. G. & Lada, C. J. 1977, ApJ, 214, 725
Feng, S., Beuther, H., Henning, T., et al. 2015, A&A, 581, A71
Foster, J. B., Jackson, J. M., Barnes, P. J., et al. 2011, ApJS, 197, 25
Garrod, R. T. 2013, ApJ, 765, 60
Garrod, R. T. & Herbst, E. 2006, A&A, 457, 927
Garrod, R. T., Wakelam, V., & Herbst, E. 2007, A&A, 467, 1103
Garrod, R. T., Weaver, S. L. W., & Herbst, E. 2008, ApJ, 682, 283
Gaume, R. A., Goss, W. M., Dickel, H. R., Wilson, T. L., & Johnston, K. J. 1995, ApJ, 438, 776
Gaume, R. A., Johnston, K. J., Nguyen, H. A., et al. 1991, ApJ, 376, 608
Gerner, T., Beuther, H., Semenov, D., et al. 2014, A&A, 563, A97
Giannetti, A., Wyrowski, F., Brand, J., et al. 2014, A&A, 570, A65
Gibb, E. L., Whittet, D. C. B., Boogert, A. C. A., & Tielens, A. G. G. M. 2004, ApJS, 151, 35
Girart, J. M., Rao, R., & Estalella, R. 2009, ApJ, 694, 56
Goddi, C., Zhang, Q., & Moscadelli, L. 2015, A&A, 573, A108
Goldsmith, P. F. & Langer, W. D. 1999, ApJ, 517, 209
Guertler, J., Henning, T., Kruegel, E., & Chini, R. 1991, A&A, 252, 801
Hatchell, J., Thompson, M. A., Millar, T. J., & MacDonald, G. H. 1998, A&A, 338, 713
Hatchell, J. & van der Tak, F. F. S. 2003, A&A, 409, 589
Henkel, C., Wilson, T. L., & Johnston, K. J. 1984, ApJ, 282, L93
Hildebrand, R. H. 1983, QJRAS, 24, 267
Hoffman, I. M., Goss, W. M., Palmer, P., & Richards, A. M. S. 2003, ApJ, 598, 1061
Hollis, J. M. 1982, ApJ, 260, 159
Hoq, S., Jackson, J. M., Foster, J. B., et al. 2013, ApJ, 777, 157
Hutawarakorn, B. & Cohen, R. J. 2003, MNRAS, 345, 175
Jackson, J. M., Rathborne, J. M., Foster, J. B., et al. 2013, PASA, 30, 57
Jiménez-Serra, I., Zhang, Q., Viti, S., Martín-Pintado, J., & de Wit, W.-J. 2012, ApJ, 753, 34
Kameya, O., Morita, K.-I., Kawabe, R., & Ishiguro, M. 1990, ApJ, 355, 562
Katz, N., Furman, I., Biham, O., Pirronello, V., & Vidali, G. 1999, ApJ, 522, 305
Kawabe, R., Suzuki, M., Hirano, N., et al. 1992, PASJ, 44, 435
Keto, E., Zhang, Q., & Kurtz, S. 2008, ApJ, 672, 423
Knez, C., Lacy, J. H., Evans, II, N. J., van Dishoeck, E. F., & Richter, M. J. 2009, ApJ, 696, 471
Kobayashi, C., Karakas, A. I., & Umeda, H. 2011, MNRAS, 414, 3231
Kraus, S., Balega, Y., Elitzur, M., et al. 2006, A&A, 455, 521
Kurtz, S. 2005, in IAU Symposium, Vol. 227, Massive Star Birth: A Crossroads of Astrophysics, ed. R. Cesaroni, M. Felli, E. Churchwell, & M. Walmsley, 111–119
Kurtz, S., Hofner, P., & Álvarez, C. V. 2004, ApJS, 155, 149
Langer, W. D. 1992, in IAU Symposium, Vol. 150, Astrochemistry of Cosmic Phenomena, ed. P. D. Singh, 193
Lee, H.-H., Roueff, E., Pineau des Forets, G., et al. 1998, A&A, 334, 1047
Lee, T. J. 1972, Nature Physical Science, 237, 99
Liu, H. B., Galván-Madrid, R., Jiménez-Serra, I., et al. 2015, ApJ, 804, 37
Lodders, K. 2003, ApJ, 591, 1220
Loren, R. B. & Mundy, L. G. 1984, ApJ, 286, 232
Lugo, J., Lizano, S., & Garay, G. 2004, ApJ, 614, 807
Mangum, J. G. & Wootten, A. 1993, ApJS, 89, 123
Martin, A. H. M. 1973, MNRAS, 163, 141
McCaughrean, M., Rayner, J., & Zinnecker, H. 1991, Mem. Soc. Astron. Italiana, 62, 715
Menten, K. M. 1991, ApJ, 380, L75
Menten, K. M., Walmsley, C. M., Henkel, C., et al. 1986, A&A, 169, 271
Minier, V., Conway, J. E., & Booth, R. S. 2001, A&A, 369, 278
Miotello, A., Testi, L., Lodato, G., et al. 2014, A&A, 567, A32
Moscadelli, L. & Goddi, C. 2014, A&A, 566, A150
Moscadelli, L., Reid, M. J., Menten, K. M., et al. 2009, ApJ, 693, 406
Mueller, K. E., Shirley, Y. L., Evans, II, N. J., & Jacobson, H. R. 2002, ApJS, 143, 469
Müller, H. S. P., Schlöder, F., Stutzki, J., & Winnewisser, G. 2005, Journal of Molecular Structure, 742, 215
Myers, P. C., Linke, R. A., & Benson, P. J. 1983, ApJ, 264, 517
Naranjo-Romero, R., Zapata, L. A., Vázquez-Semadeni, E., et al. 2012, ApJ, 757, 58
Öberg, K. I., Linnartz, H., Visser, R., & van Dishoeck, E. F. 2009, ApJ, 693, 1209
Ojha, D. K., Tamura, M., Nakajima, Y., et al. 2004, ApJ, 616, 1042
Olmi, L., Cesaroni, R., & Walmsley, C. M. 1993, in Bulletin of the American Astronomical Society, Vol. 25, American Astronomical Society Meeting Abstracts, 1315
Ossenkopf, V. & Henning, T. 1994, A&A, 291, 943
Palau, A., Fuente, A., Girart, J. M., et al. 2011, ApJ, 743, L32
Penzias, A. A. 1980, in IAU Symposium, Vol. 87, Interstellar Molecules, ed. B. H. Andrew, 397–402
Pestalozzi, M. R., Elitzur, M., & Conway, J. E. 2009, A&A, 501, 999
Pestalozzi, M. R., Elitzur, M., Conway, J. E., & Booth, R. S. 2004, ApJ, 603, L113
Pestalozzi, M. R., Minier, V., Motte, F., & Conway, J. E. 2006, A&A, 448, L57
Pickett, H. M., Poynter, R. L., Cohen, E. A., et al. 1998, J. Quant. Spec. Radiat. Transf., 60, 883
Pineau des Forets, G., Roueff, E., Schilke, P., & Flower, D. R. 1993, MNRAS, 262, 915
Plambeck, R. L. & Menten, K. M. 1990, ApJ, 364, 555
Pratap, P., Batrla, W., & Snyder, L. E. 1989, ApJ, 341, 832
Pratap, P., Snyder, L. E., & Batrla, W. 1992, ApJ, 387, 241
Qiu, K. & Zhang, Q. 2009, ApJ, 702, L66
Qiu, K., Zhang, Q., & Menten, K. M. 2011, ApJ, 728, 6
Russeil, D., Zavagno, A., Motte, F., et al. 2010, A&A, 515, A55
Sanchez-Monge, A. 2011, PhD thesis, University of Barcelona
Sandell, G., Goss, W. M., Wright, M., & Corder, S. 2009, ApJ, 699, L31
Sandell, G. & Sievers, A. 2004, ApJ, 600, 269
Sandell, G. & Wright, M. 2010, ApJ, 715, 919
Sandell, G., Wright, M., & Forster, J. R. 2003, ApJ, 590, L45
Sanhueza, P., Jackson, J. M., Foster, J. B., et al. 2012, ApJ, 756, 60
Schuller, F., Menten, K. M., Contreras, Y., et al. 2009, A&A, 504, 415
Scoville, N. Z., Sargent, A. I., Sanders, D. B., et al. 1986, ApJ, 303, 416
Semenov, D., Hersant, F., Wakelam, V., et al. 2010, A&A, 522, A42
Semenov, D. & Wiebe, D. 2011, ApJS, 196, 25
Sobolev, A. M., Cragg, D. M., Ellingsen, S. P., et al. 2007, in IAU Symposium, Vol. 242, IAU Symposium, ed. J. M. Chapman & W. A. Baan, 81–88
Sutton, E. C., Sobolev, A. M., Salii, S. V., et al. 2004, ApJ, 609, 231
Tackenberg, J., Beuther, H., Henning, T., et al. 2012, A&A, 540, A113
Tan, J. C., Beltrán, M. T., Caselli, P., et al. 2014, Protostars and Planets VI, 149
van der Tak, F. F. S., Black, J. H., Schöier, F. L., Jansen, D. J., & van Dishoeck, E. F. 2007, A&A, 468, 627
van der Tak, F. F. S., van Dishoeck, E. F., Evans, II, N. J., & Blake, G. A. 2000, ApJ, 537, 283
van Dishoeck, E. F. 2009, Astrochemistry of Dense Protostellar and Protoplanetary Environments, ed. H. A. Thronson, M. Stiavelli, & A. Tielens, 187
van Dishoeck, E. F., Jonkheid, B., & van Hemert, M. C. 2006, Faraday Discussions, 133, 231
Voronkov, M. A., Brooks, K. J., Sobolev, A. M., et al. 2006, MNRAS, 373, 411
Wang, K., Zhang, Q., Testi, L., et al. 2014, MNRAS, 439, 3275
Werner, M. W., Becklin, E. E., Gatley, I., et al. 1979, MNRAS, 188, 463
Willner, S. P. 1976, ApJ, 206, 728
Willner, S. P., Gillett, F. C., Herter, T. L., et al. 1982, ApJ, 253, 174
Wilson, T. L., Rohlfs, K., & Hüttemeister, S. 2009, Tools of Radio Astronomy (Springer-Verlag)
Wilson, T. L. & Rood, R. 1994, ARA&A, 32, 191
Wilson, T. L., Walmsley, C. M., Batrla, W., & Mauersberger, R. 1983, A&A, 127, L19
Wilson, T. L., Walmsley, C. M., Jewell, P. R., & Snyder, L. E. 1984, A&A, 134, L7
Wright, M., Zhao, J.-H., Sandell, G., et al. 2012, ApJ, 746, 187
Wright, M. C. H., Hull, C. L. H., Pillai, T., Zhao, J.-H., & Sandell, G. 2014, ApJ, 796, 112
Wright, M. C. H., Plambeck, R. L., & Wilner, D. J. 1995, Astronomy Data Image

Library, 2
Wynn-Williams, C. G., Becklin, E. E., & Neugebauer, G. 1974, ApJ, 187, 473
Zapata, L. A., Schmid-Burgk, J., Ho, P. T. P., Rodríguez, L. F., & Menten, K. M. 2009, ApJ, 704, L45
Zeng, Q., Mao, P. Q., & Pei, C. C. 2006, Microwave spectrum of astrophysics diagnosis (Chinese edition)
Zhang, Q., Ho, P. T. P., & Ohashi, N. 1998, ApJ, 494, 636
Zhang, Q., Hunter, T. R., Beuther, H., et al. 2007, ApJ, 658, 1152
Zhang, Q., Wang, Y., Pillai, T., & Rathborne, J. 2009, ApJ, 696, 268
Zheng, X.-W., Zhang, Q., Ho, P. T. P., & Pratap, P. 2001, ApJ, 550, 301
Zhu, L., Zhao, J.-H., Wright, M. C. H., et al. 2013, ApJ, 779, 51
Zinnecker, H. & Yorke, H. W. 2007, ARA&A, 45, 481

Appendix A: An iterative approach to obtain the opacity corrected rotational temperature of CH_3CN

CH_3CN is a symmetric-top molecule with no dipole moment perpendicular to the molecular axis, and its K-ladders in rotational levels can be excited solely by collisions, so it is a good temperature tracer in dense cloud. The traditional rotation diagram method is based on the following assumption: (1) The collision rates of CH_3CN are sufficient to thermalize the rotational levels, i.e. in local thermodynamic equilibrium (LTE); (2) All lines originate from the same parcels of gas along the line of sight; (3) All lines are optically thin; (4) All lines have the same velocity and a single temperature. Therefore, the rotational excitation temperature T_{rot} is equal to the kinetic temperature, and the level populations are then directly proportional to the line intensities of the K components. (Boucher et al. 1980; Hollis 1982; Loren & Mundy 1984; Olmi et al. 1993; Wright et al. 1995; Goldsmith & Langer 1999; Zhang et al. 1998).

Our observation band covers the J=12-11 transitions of CH_3CN around 220 GHz, with upper state energy levels E_u/k spanning from ~ 70 K to ~ 500 K, yielding a large range for determining temperature. With the detected lines listed in Table A3, we derive the T_{rot} and the column density N_T of CH_3CN in each substructure (Figure 4, purple dashed lines in Panel 1–2, black fit in Panel 3–4). The fitted synthetic spectrum (Sanchez-Monge 2011; Palau et al. 2011, see also Section 4.2.1) deviates from the observations, especially at K = 0, 1, 2, 3, 6, and the reasons are multiple: (1) the K = 3, 6 lines are from ortho (o-) transitions, which has forbidden collisional transition with the other para (p-) lines, so they are treated to be two different molecules (Andersson et al. 1984). (2) K = 0, 1 lines are blended, so estimation of their integrated intensity derived by simply taking into account their relative weights is uncertain; (3) K = 0, 1, 2 lines are optically thick, which is the main issue (Feng et al. 2015).

Compared to CH_3CN, lines of its rare isotopologue $CH_3^{13}CN$ should be optically thin. However, $CH_3^{13}CN$ ($12_2 \rightarrow 11_2$) is the only transition that is not blended with the broad line wings of CH_3CN. We use the following iterative approach to derive the opacity corrected rotational temperature T_{rot} of MM1, MM2, and IRS1-mmS (red solid fittings in Panels 3–5 of Figure 4):

(1) Obtain the rotational temperature T_1 without any opacity correction;
(2) Estimate the optical depth of CH_3CN ($12_2 \rightarrow 11_2$) $\tau_{K,1\ (K=2)}$ by comparing its main beam temperature with that of $CH_3^{13}CN$ ($12_2 \rightarrow 11_2$), and calculate the column density of line $12_2 \rightarrow 11_2$ at T_1 with the optical depth correction. Then, estimate the total column density of CH_3CN as N_1 assuming LTE (see Appendix B for more details about the correction);
(3) With T_1 and N_1 as trial input parameters, estimate the optical depth for the remaining transitions in the CH_3CN ladder $\tau_{K,1\ (K=0-8)}$ with the RADEX code package[19] (van der Tak et al. 2007), then correct their column densities line by line (dots and triangles in red in Figure 4) and obtain a new rotational temperature T_2;
(4) Repeat step (2)–(3) until $(|T_n - T_{n-1}|)/T_{n-1} \leq 10\%$ (n=2,3,...; see fittings in red in Figure 4).

In reality, molecules are not distributed homogeneously in the clouds, and they are far from being homogeneous in density and temperature. The ultimate best-fit requires a sophisticated, fully 3-D physico-chemo long-range transport modelling, which is beyond the scope of our paper.

Appendix B: Spectral line column density estimates

For all the species we detected, we calculate their column densities (from both main and rare isotopologues) from the integrated spectral line intensities as below.

The optical depth τ_υ (in velocity) along the line of sight is (Zeng et al. 2006, Eq. A.25):

$$\tau_\upsilon = \frac{c^3}{8\pi\nu^3} A_{ul} N_u (e^{\frac{h\nu}{k_B T_{rot}}} - 1)\Phi(\upsilon). \quad (B.1)$$

where c is the speed of light, k_B the Boltzmann constant, h the Planck constant, ν the line rest frequency, $\Phi(\upsilon)$ the distribution function of the line shape in terms

[19] RADEX is a one-dimensional non-LTE radiative transfer code, providing an alternative to the widely used rotation diagram method. Without requiring the observation of many optically thin emission lines, it can be used to roughly constrain the excitation temperature in addition to the column density.

of velocity υ. Here, A_{ul} is the average spontaneous emission rate from the upper state E_u into the lower state E_l, and it is calculated from line strength S_{ul} and dipole moment μ as

$$A_{ul} = \frac{64\pi^4\nu^3}{3hc^3}\frac{S_{ul}\mu^2}{g_u} \tag{B.2}$$

After integrating the optical depth over the observed linewidth, $\int\Phi(\upsilon)d\upsilon = 1$, and the column density N_u of the line at ν Hz is

$$N_u = \frac{8\pi\nu^3}{c^3 A_{ul}}\frac{1}{\exp(\frac{h\nu}{k_B T_{rot}})-1}\int\tau_\upsilon d\upsilon. \quad (cm^{-2}) \tag{B.3}$$

When assuming LTE, the total column density of all transitions for a molecule α is

$$N_{T,\alpha} = \frac{N_u}{g_u}Q(T_{rot})e^{\frac{E_u}{k_B T_{rot}}} \quad (cm^{-2}) \tag{B.4}$$

where $Q(T_{rot})$ is the partition function for the given (rotational) excitation temperature of each sources, which is interpolated from a table of partition functions for fixed temperatures, obtained from CDMS/JPL.

Here, $S_{ul}\mu^2$ can be calculated from the CDMS/JPL line intensity $\ell(T_{rot})$ (Pickett et al. 1998),

$$\begin{aligned} S_{ul}\mu^2 &= \frac{3hc}{8\pi^3\nu}\ell(T_{rot})Q(T_{rot})(e^{-\frac{E_l}{k_B T_{rot}}} - e^{-\frac{E_u}{k_B T_{rot}}})^{-1} && \text{(B.5)}\\ &= 2.4025\times10^{10}[\frac{\nu}{Hz}]^{-1}[\frac{\ell(300\,K)}{nm^2 MHz}]Q(300K) \\ &\quad \times[e^{-\frac{E_l}{k_B 300K}} - e^{-\frac{E_u}{k_B 300K}}]^{-1} Debye^2 && \text{(B.6)}\end{aligned}$$

The spectra from NGC 7538 S consist of pure emission lines, while spectrum from the IRS1-peak is a mixture of emission and absorption lines. Accordingly, we calculate the line column densities separately for these two cases.

1. For absorption lines in IRS1-peak, the optical depth can be calculated from the flux intensity ratio between a particular line F_υ and the continuum $F_{\upsilon,c}$, $\tau_\upsilon = -\ln(F_\upsilon/F_{\upsilon,c})$. Then, Eq. B.4 yields:

$$N_{T,\alpha} = \frac{8\pi\nu}{\ell(T_{rot})\eta c^3}\int\tau_\upsilon d\upsilon \qquad (cm^{-2}) \qquad \text{(absorption)} \tag{B.7}$$

2. For the emission lines, we assume the Rayleigh-Jeans approximation ($\frac{h\nu}{k_B T_{rot}} \ll 1$), therefore Eqs. B.3 and B.4 can be simplified as (Zeng et al. 2006, Eq. 4.26, also see Wilson et al. 2009),

$$\begin{aligned} &\frac{N_u}{g_u} \cong \frac{3k_B}{8\pi^3\nu S_{ul}\mu^2}T_{rot}\int\tau_\upsilon d\upsilon \qquad (cm^{-2}) \\ &N_{T,\alpha} = \frac{k_B}{hc}\frac{(e^{\frac{h\nu}{k_B T_{rot}}}-1)}{\ell(T_{rot})}T_{rot}\int\tau_\upsilon d\upsilon \qquad (cm^{-2}) \end{aligned} \quad \text{(emission)} \tag{B.8}$$

Assuming that the observed emission in each substructure is homogeneous and fills the beam, the integration of measured main beam brightness temperature within the velocity range $\int T_B(\upsilon)d\upsilon$ can be substituted for the last term in the above equation:

$$T_{rot}\int\tau_\upsilon d\upsilon \cong \frac{\tau_{\alpha,0}}{1-e^{-\tau_{\alpha,0}}}\int T_B(\upsilon)d\upsilon \qquad (K\,cm\,s^{-1}) \tag{B.9}$$

where $\tau_{\alpha,0}$ is the optical depth at line centre, and $\int T_B(\upsilon)d\upsilon$ is measured from Gaussian/hyperfine structure (HFS) fit by using the Gildas software package.

The column densities and related uncertainties of species listed in Table A5 (CH_3CN and HNCO) can be estimated directly from their rotation diagrams and the scatterings of the data points (Figure 4). For the species whose transitions are not sufficient to derive the rotation diagrams, we estimate their column densities by assuming that their transitions have the same T_{rot} as those derived from the opacity-corrected CH_3CN.

In general, we assume that the observed transitions are optically thin ($\tau_{\alpha,0} \le 1$, $\frac{\tau_{\alpha,0}}{1-e^{-\tau_{\alpha,0}}} \approx 1$). However, for several molecules with large abundances, we observe the corresponding transitions of their main and rare isotopologues. By measuring the ratio between main beam brightness temperature of the main line $T_{B,\,\alpha,0}$ and its rare isotopologue $T_{B,\,\beta,0}$, we can estimate the optical depth at line centre of a given transition $\tau_{\alpha,0}$ (Myers et al. 1983):

$$\frac{1-\exp(-\tau_{\alpha,0}/\mathfrak{R}^\alpha)}{1-\exp(-\tau_{\alpha,0})} \approx \frac{T_{B,\,\beta,0}}{T_{B,\,\alpha,0}} \tag{B.10}$$

where $\mathfrak{R}_\alpha$ is the intrinsic abundance of the main isotope (e.g. ^{12}C) compared to its rare isotope (e.g. ^{13}C) in the ISM (Table C.1, e.g. Wilson & Rood 1994; Chin et al. 1996).

Appendix C: Error budget in observed parameters and modelling fits

Various assumptions must be made in order to estimate observed molecular abundances and best-fits from modelling. Below we consider the main assumptions in the method and how they affect the resulting values.

C.1. Rotational Temperature

We adopt the gas temperature derived from the opacity corrected rotation diagrams of CH_3CN in MM1, MM2, and IRS1-mmS. To verify these T_{rot}, we compare them with the temperatures derived from previous studies.

Our temperatures in MM1 and MM2 are slightly higher than derived from unresolved observations, for example Zheng et al. (2001) (~ 25 K from NH_3) and Sandell & Wright (2010) (52 ± 10 K from $H^{13}CN$, DCN, and CH_3CN). However, this is expected as we are able to resolve localized warm gas concentrations on 0.01 pc-scale.

We also find a slightly warmer temperature for IRS1-mmS (~ 160 K) than the cm observations of Goddi et al. 2015 (~ 120 K), although this is likely due to their cm observations and our mm observations tracing different components (with offset $\triangle\alpha \sim 1''$). The temperature towards IRS1-peak (~ 214 ± 66 K) is assumed by taking the measurement towards IRS1-mmS as the lower limit and that from Goddi et al. (2015) as upper limit, so it is consistent with the temperature measured towards the entire IRS1, for example, from an LVG fit of CH_3CN by Qiu et al. (2011) (245 ± 25 K) and by Zhu et al. (2013) (~ 260 K).

C.2. Molecular Column Densities

We found that the abundance ratios in between the main and rare isotopologues are consistent with the isotope ratio in the local ISM (e.g. SO, ^{13}CO, OCS, and CH_3CN in Table. C.1). However, there are some uncertainties which might impact our estimation:

The isotopic S-elements ratio in NGC 7538 is assumed to be close to the ratio of the solar system (e.g. $^{32}S/^{33}S = 127$, Lodders 2003). However, solar system values might have a bias since the Galactic disk outside the solar system is affected by isotope changes (e.g. Kobayashi et al. 2011). Observationally, $^{32}S/^{33}S$ is expected in the range 100–210 at the galactocentric distance of NGC 7538 (e.g. Chin et al. 1996). Therefore, a more precise opacity correction for SO line requires a more accurate local $^{32}S/^{33}S$ ratio.

Fractionation reactions can also produce changes in the main/rare isotopologue ratios, in particular via exchange reactions[20] involving $^{12}C \Leftrightarrow ^{13}C$ (Penzias 1980; Langer 1992), $^{16}O \Leftrightarrow ^{18}O$, and $^{32}S \Leftrightarrow ^{33}S \Leftrightarrow ^{34}S$.

We assume that emission lines of the same species (including all isotopologues) have the same excitation temperature, which is often not the case. In these dense, warm gas condensations with strong background IR dust thermal emission, it is possible that some of the lines, especially for COMs, are weakly masing, i.e. their intensities depart from LTE (S. Parfenov, priv. comm.). The degree of these differences are a factor of a few at most (see the scatter of the data points in Figure 4). Therefore, a more accurate calculation requires proper chemical modelling and LVG calculation.

In brief, our analytic calculations suggest that an uncertainty in optical depth dominates the uncertainty in the derived molecular column densites. Without the opacity correction, molecular column densities are on average underestimated by a factor of 5–10 (Figure 5). For abundant species such as

[20] Exchange reactions of $^{16}O \Leftrightarrow ^{18}O$ and $^{32}S \Leftrightarrow ^{33}S \Leftrightarrow ^{34}S$ have been found in AGB star, PDR, and meteoritic records.

Table C.1: Optical depths and abundance ratios for SO, ^{13}CO, OCS, and CH_3CN lines with respect to their rare isotopologue lines in each substructure of NGC 7538S and IRS1-mmS

Species		$\mathfrak{R}_\alpha$	MM1 (172 ± 23 K)	MM2 (137 ± 14 K)	MM3 (50 K)	JetN (150 K)	JetS (150 K)	IRS1 – mmS (162 ± 14 K)
$\tau_{SO\ (6_5\rightarrow5_4)}$			44.5	7.5	–	≤ 24	≤ 6.5	10
$N_{SO_\tau}/N_{^{33}SO}$	†	127	$112.20_{\pm0.96}$	$94.46_{\pm10.42}$	––	≤ 638.08	≤ 409.18	$132.30_{\pm21.26}$
$N_{SO}/N_{^{33}SO}$	⋆		$2.52_{\pm0.02}$	$12.59_{\pm1.39}$	–	≥ 26.59	≥ 62.86	$13.23_{\pm2.13}$
$\tau_{^{13}CO\ (2\rightarrow1)}$			13.5	9	≥ 9	8	8	––
$N_{^{13}CO_\tau}/N_{C^{18}O}$	†	8.3	$16.07_{\pm0.52}$	$17.58_{\pm0.02}$	≥ 12.54	$13.84_{\pm0.52}$	$16.00_{\pm0.95}$	––
$N_{^{13}CO}/N_{C^{18}O}$	⋆		$1.19_{\pm0.04}$	$1.95_{\pm0.00}$	≤ 1.39	$1.73_{\pm0.06}$	$2.00_{\pm0.12}$	––
$\tau_{OCS\ (18\rightarrow17)}$			4.5	5.5	36	≤ 38	15	4
$N_{OCS_\tau}/N_{O^{13}CS}$	†	73.5	$76.71_{\pm1.88}$	$72.81_{\pm16.34}$	$69.24_{\pm1.17}$	≤ 159.60	≤ 72.06	$86.40_{\pm27.69}$
$N_{OCS}/N_{O^{13}CS}$	⋆		$16.86_{\pm0.41}$	$13.18_{\pm2.96}$	$1.92_{\pm0.03}$	≥ 4.20	≥ 4.80	$21.20_{\pm6.80}$
$\tau_{CH_3CN\ (12_2\rightarrow11_2)}$			16	3	≤29	–	–	7
$N_{CH_3CN_\tau}/N_{CH_3^{13}CN}$	†	73.5	$70.22_{\pm7.06}$	$78.13_{\pm2.02}$	≤ 119.60	––	––	$71.88_{\pm5.30}$
$N_{CH_3CN}/N_{CH_3^{13}CN}$	⋆		$4.39_{\pm0.44}$	$24.75_{\pm0.64}$	≥ 4.12	––	––	$10.26_{\pm0.76}$

Note.
1) † or ⋆ mark the estimations with or without optical depth correction, respectively.
2) ≥ (≤) come from the 3σ limit of the non-detection or partly absorption of $C^{18}O$ in IRS1-mmS.
3) The ratios $\mathfrak{R}_\alpha$ between isotopes of $^{12}C/^{13}C$ and $^{16}O/^{18}O$ are provided from the Galactic ISM ratio measured in Giannetti et al. (2014) (with R_{GC}(NGC 7538) ~ 9.7 kpc), while $^{32}S/^{33}S$ is provided from the solar system ratio measured in Lodders (2003).
4) Uncertainties on the measured values are typically ≤ 10% as determined from T_{rot}, partition function $Q(T_{rot})$, and Gaussian fit to $T_B(\upsilon)d\upsilon$.

HNCO, HC_3N, and SO_2, for which we do not observe corresponding transitions of their rare isotopologues (marked with † in Table. 4), our assumption that their strongest lines are optically thin may result in an underestimation by a similar factor. Furthermore, when we derive the molecular column density from only one line, uncertainty about the level of thermalization will result in an uncertainty on the resulting column density on the order of <20% (estimated from the scatter of CH_3CN and HNCO rotation diagrams). In addition to these, uncertainties of T_{rot} and line intensity integration are negligible compared to the chemical variation among the substructures (on average < 10%, written in subscript in Tables A4–A5).

C.3. N_{H_2} and Molecular Abundances

H_2 column densities are calculated using two methods: from dust continuum ($N_{H_{2,1}}$) as in MM1–MM3, and from $C^{18}O$ ($N_{H_{2,2}}$) as in all substructures of NGC 7538 S and IRS1 as described in Section 5.2.2. We found $N_{H_{2,2}}/N_{H_{2,1}}$ is ~ 0.98 in MM1, ~ 0.16 in MM2, but only 0.006 in MM3. Several reasons may lead to these differences:

1. Since dust properties are unknown, we simply assume that the number densities in condensations MM1–MM3 are the same (10^8 cm^{-3}), and that the gas distribution within each condensation is homogeneous. Therefore we expect the gas-to-dust ratio (~ 150) and the dust opacity to be the same across all three condensations. However, grain properties, such as the thickness of the ice mantle, can vary strongly along the line of sight, resulting in differences in derived H_2 column densities.

2. Difference in grain growth between the envelopes can result in differing dust emissivities (e.g. Miotello et al. 2014).

3. A constant relative abundance of $C^{18}O$ to H_2 may not be true and would strongly affect the derived $N_{H_{2,2}}$. A varying value could be caused by changes in the optical depth of the $C^{18}O$ line, isotopic-selective depletion effects or simply $C^{18}O$ and dust tracing different regions within the condensations.

With these in consideration, molecular abundances with respect to H_2 in MM1–MM3 are more reliable when N_{H_2} is derived from the dust continuum.

C.4. Short Spacings

Without short spacings, our interferometric data can lead to underestimated column densities, especially in the extended regions JetS and JetN due to filtering out flux. Compared to the specific intensity extrapolated from the single-dish 1.2 mm MAMBO data (Sandell & Sievers 2004), we estimate that 48% of the flux has been filtered out from IRS1 and 90% of flux from NGC 7538 S (Beuther et al. 2012), suggesting that emission from NGC 7538 S is more extended than that from IRS1. Since the fraction of filtered-out flux should be lower at the center of the primary beam, uncertainties in column densities are larger in the outflow of NGC 7538 S than in the dense condensations MM1–MM3.

C.5. Local Thermal Equilibrium

We have assumed all molecules are in LTE, however this is likely not the case for some species. An indication of this case is that SO has differing brightness and rotational temperatures in MM1 (T_{rot} ~ 170 K but T_B ~ 30 K). This dichotomy could be explained by: (1) SO is absorbed in the colder mantle which has not been resolved in our observations; or (2) the liberation of SO from grains by shocks and thus be non-LTE excited. Without higher spatial resolution observations of the substructures within each condensation, we are unable to distinguish between clumpiness, non-LTE effects or the beam dilution which causes this inconsistency.

C.6. The modelling fits

Table. 4 and Figure 6 show that 60%-70% of the modelled molecular column densities agree with the observed values within the quoted uncertainties. Several sources relate to our model fitting procedure may bring uncertainties and disagreement with the observations.

The effects of shocks have not been included in our models. The $N_{observed}$ of SO_2 is at least 1-2 magnitudes lower than the $N_{modelled}$ in MM2 and MM3. MM1 shows $N_{observed}$ of SO_2 is higher than $N_{modeled}$ by a factor of 10. The significantly enhanced gas phase SO_2 in MM1 may be related to the associated stronger shocks (Pineau des Forets et al. 1993; Bachiller & Pérez Gutiérrez 1997; Garrod 2013) produced by outflows detected around MM1.

In addition, our model contains many assumptions which may affect the resulting fit. Chemical models are hugely sensitive to initial conditions. In the above framework we have assumed that our best-fit MM3 model provides the initial conditions for the following two evolutionary stages. However, with many non-detections in MM3, the initial conditions were based on upper limits and so they may not be entirely correct. It most be noted however that the problem of initial conditions is ubiquitous among all chemical models. Furthermore, photodissociation rates for COMs can be uncertain by factors of 10 – 100 which will greatly affect the resulting column densities. Finally, a spherically symmet-

ric source is the limit of a 1-D model. Velocity gradients across both MM1 and MM2 indicate rotation, suggesting a disk-like morphology (Beuther et al. 2012). In such a scenario one would find much higher densities and therefore much shorter timescales for chemical processes.

Table A1. Identified lines from PdBI dataset. In case of blending, lines with stronger CDMS/JPL intensity are listed in the left column, and the possible weaker blended transitions in the right column.

Freq.[a] (GHz)	Mol[b]	Trans.[c]	E_u/k (K)	Cmt.[d]	Freq.[a] (GHz)	Mol.[d] (candidates)	Trans.[c]	E_u/k (K)	Cmt.[d]
217.19 ± 0.01	UL			2.2	217.191	CH_3OCH_3	$(22_{4,19}-22_{3,20})$A(E)A(E)	253	
					217.194	$g-(CH_2OH)_2(v=1)$	$(17_{4,14}\rightarrow 16_{3,13})$	83	
					217.194	$HCOOCH_{3(v=0)}$	$(30_{4,26}\rightarrow 30_{3,27})$E	291	
217.216	$HCOOCH_{3(v=0)}$	$(32_{9,24}\rightarrow 32_{8,25})$A	368	1.3					
217.236*	$HCOOCH_{3(v=0)}$	$(32_{9,24}\rightarrow 32_{8,25})$E	368	1.3					
217.239	DCN	$(3\rightarrow 2)$	21	†					
217.3 ± 0.01	UL			2.2	217.300	$CH_2^{13}CHCN$	$(23_{5,19}\rightarrow 22_{5,18})$	178	
					217.301	$CH_2^{13}CHCN$	$(23_{5,18}\rightarrow 22_{5,17})$	178	
					217.290-217.307	^{13}CN	(N = 2 − 1)	16	
					217.299	$CH_3OH_{(v_t=1)}$	$(6_{1,5}\rightarrow 7_{2,6}--)$	374	
217.313	$HCOOCH_{3(v=1)}$	$(17_{4,13}\rightarrow 16_{4,12})$A	290	1.2					
217.64 ± 0.01	UL			2.2	217.639	$^{13}CH_3CH_2CN$	$(25_{1,24}\rightarrow 24_{1,23})$	139	
					217.642	$CH_2CH^{13}CN$	$(23_{4,19}\rightarrow 22_{4,18})$	160	
					217.646	$CH_2^{13}CHCN$	$(23_{14,9}\rightarrow 22_{14,8})$	533	
					217.646	$CH_2^{13}CHCN$	$(23_{14,10}\rightarrow 22_{14,9})$	533	
					217.633-217.640	^{13}CN	(N = 2 − 1)	15	
					217.643	$CH_3OH_{(v_t=1)}$	$(15_{6,10}\rightarrow 16_{5,11}--)$	746	
					217.643	$CH_3OH_{(v_t=1)}$	$(15_{6,9}\rightarrow 16_{5,12}++)$	746	
217.833	^{33}SO	$(6_5\rightarrow 5_4)$	35	†					
217.89 ± 0.005	UL			2.2	217.886	$CH_3OH_{(v_t=0)}$	$(20_{1,19}\rightarrow 20_{0,20})$	508	
					217.889	$CH_2CH^{13}CN$	$(23_{14,9}\rightarrow 22_{14,8})$	544	
					217.889	$CH_2CH^{13}CN$	$(23_{14,10}\rightarrow 22_{14,9})$	544	
					217.895	$^{13}CH_2CHCN$	$(23_{1,23}\rightarrow 22_{0,22})$	121	
218.108	$HCOOCH_{3(v=1)}$	$(17_{4,13}\rightarrow 16_{4,12})$E	290	1.2					
218.198*	$O^{13}CS$	$(18\rightarrow 17)$	99	3 †					
218.222	H_2CO	$(3_{0,3}\rightarrow 2_{0,2})$	21						
218.260	$HCOOCH_{3(v=0)}$	$(31_{9,23}\rightarrow 31_{8,24})$A	349	1.3					
218.281	$HCOOCH_{3(v=0)}$	$(17_{3,14}\rightarrow 16_{3,13})$E	100	2.2					
218.298	$HCOOCH_{3(v=0)}$	$(17_{3,14}\rightarrow 16_{3,13})$A	100	2.2					
218.325	$HC_3N_{(v=0)}$	$(24\rightarrow 23)$	131	†					
218.390	$CH_3CH_2CN_{(v=0)}$	$(24_{3,21}\rightarrow 23_{3,20})$	140	3 †					
218.440	$CH_3OH_{(v=0)}$	$(4_{2,2}\rightarrow 3_{1,2})$	46	†					
218.460	NH_2CHO	$(10_{1,9}\rightarrow 9_{1,8})$	61	†					
218.476	H_2CO	$(3_{2,2}\rightarrow 2_{2,1})$	68	†					
218.585*	$HCOOCH_{3(v=0)}$	$(36_{9,28}\rightarrow 36_{8,29})$A	450	2.2					
218.593*	$HCOOCH_{3(v=0)}$	$(27_{7,21}\rightarrow 27_{5,22})$A	258	2.2					
218.607*	$HCOOCH_{3(v=0)}$	$(36_{9,28}\rightarrow 36_{8,29})$E	450	2.2					
218.633*	$HCOOCH_{3(v=0)}$	$(27_{7,21}\rightarrow 27_{5,22})$E	258	2.2					
218.655	$HCOOCH_{3(v=1)}$	$(18_{16,2}\rightarrow 17_{16,1})$E	460	1.3					
218.738	$HCOOCH_{3(v=1)}$	$(18_{14,4}\rightarrow 17_{14,3})$E	419	2.3					
218.760	H_2CO	$(3_{2,1}\rightarrow 2_{2,0})$	68						
218.831	$HCOOCH_{3(v=1)}$	$(18_{13,5}\rightarrow 17_{13,4})$E	401	1.3					
218.861	$HC_3N_{(v_7=1)}$	$(24\rightarrow 23, l=1e)$	452	†					
218.903	$OCS_{(v=0)}$	$(18\rightarrow 17)$	100	†					
218.966	$HCOOCH_{3(v=1)}$	$(18_{12,6}\rightarrow 17_{12,5})$E	384	1.3					
218.981	$HNCO_{(v=0)}$	$(10_{1,10}\rightarrow 9_{1,9})$	101	†					
219.068*	$HCOOCH_{3(v=1)}$	$(18_{17,2}\rightarrow 17_{17,1})$E	481	2.2					
219.079*	$HCOOCH_{3(v=1)}$	$(28_{3,25}\rightarrow 28_{2,26})$E	434	2.2					
219.090*	$HCOOCH_{3(v=0)}$	$(34_{7,28}\rightarrow 34_{5,29})$E	388	2.2					
219.109*	$HCOOCH_{3(v=0)}$	$(34_{7,28}\rightarrow 34_{5,29})$A	388	2.3					
219.153*	$HCOOCH_{3(v=1)}$	$(10_{4,6}\rightarrow 9_{3,6})$E	230	2.3	219.155*	$HCOOCH_{3(v=1)}$	$(18_{11,7}\rightarrow 17_{11,6})$E	369	2.3
219.174	$HC_3N_{(v_7=1)}$	$(24\rightarrow 23)$	452						
219.195*	$HCOOCH_{3(v=1)}$	$(18_{16,3}\rightarrow 17_{16,2})$E	459	2.3					
219.264*	$HCOOCH_{3(v=0)}$	$(36_{6,30}\rightarrow 36_{6,31})$A	429	2.2					
219.276	$SO_{2(v=0)}$	$(22_{7,15}\rightarrow 23_{6,18})$	352	†					
219.331*	$HCOOCH_{3(v=1)}$	$(18_{15,4}\rightarrow 17_{15,3})$E	438	2.3					
219.355	$^{34}SO_{2(v=0)}$	$(11_{1,11}\rightarrow 10_{0,10})$	60	3 †					
219.412	$HCOOCH_{3(v=1)}$	$(18_{10,8}\rightarrow 17_{10,7})$E	355						
219.417*	$HCOOCH_{3(v=0)}$	$(30_{5,26}\rightarrow 30_{4,27})$E	292	2.3					
219.479	$HCOOCH_{3(v=1)}$	$(18_{14,5}\rightarrow 17_{14,4})$E	419	2.3					
219.484*	$HCOOCH_{3(v=0)}$	$(30_{5,26}\rightarrow 30_{4,27})$A	292	2.3					
219.506	$CH_3CH_2CN_{(v=0)}$	$(24_{2,22}\rightarrow 23_{2,21})$	136	2.3					
219.560	$C^{18}O$	$(2\rightarrow 1)$	16	†					
219.566	$HCOOCH_{3(v=1)}$	$(18_{14,4}\rightarrow 17_{14,3})$A	419		219.566	$HCOOCH_{3(v=1)}$	$(18_{14,5}\rightarrow 17_{14,5})$A	419	
					219.566	$HCOOCH_{3(v=1)}$	$(18_{15,4}\rightarrow 17_{15,3})$A	438	
					219.566	$HCOOCH_{3(v=1)}$	$(18_{15,3}\rightarrow 17_{15,3})$A	438	
					219.571	$HCOOCH_{3(v=1)}$	$(18_{16,2}\rightarrow 17_{16,1})$A	459	
					219.571	$HCOOCH_{3(v=1)}$	$(18_{16,3}\rightarrow 17_{16,2})$A	459	
219.579	$HCOOCH_{3(v=0)}$	$(28_{9,19}\rightarrow 28_{8,20})$A	295	2.3					
219.584	$HCOOCH_{3(v=1)}$	$(18_{13,5}\rightarrow 17_{13,4})$A	401	2.3	219.584	$HCOOCH_{3(v=1)}$	$(18_{13,6}\rightarrow 17_{13,5})$A	401	2.3
219.592	$HCOOCH_{3(v=0)}$	$(28_{9,19}\rightarrow 28_{8,20})$E	295	1.3					
219.600	$HCOOCH_{3(v=0)}$	$(30_{9,22}\rightarrow 30_{8,23})$E	330	1.1					
219.607	$HCOOCH_{3(v=0)}$	$(30_{5,26}\rightarrow 30_{3,27})$E	292						
219.623	$HCOOCH_{3(v=1)}$	$(18_{12,6}\rightarrow 17_{12,5})$A	384	1.1	219.623	$HCOOCH_{3(v=1)}$	$(18_{12,7}\rightarrow 17_{12,6})$A	384	1.1
219.642	$HCOOCH_{3(v=1)}$	$(18_{13,6}\rightarrow 17_{13,5})$E	400	1.1					
219.657*	HNCO	$(10_{3,8}\rightarrow 9_{3,7})$	447		219.657	HNCO	$(10_{3,7}\rightarrow 9_{3,6})$	447	
219.696	$HCOOCH_{3(v=1)}$	$(18_{11,8}\rightarrow 17_{11,7})$A	369	1.3	219.696	$HCOOCH_{3(v=1)}$	$(18_{11,7}\rightarrow 17_{11,6})$A	369	1.3
219.705	$HCOOCH_{3(v=1)}$	$(18_{4,15}\rightarrow 17_{4,14})$A	299	2.2					

219.734*	$HNCO_{(v=0)}$	$(10_{2,9} \rightarrow 9_{2,8})$	231		219.737	$HNCO_{(v=0)}$	$(10_{2,8} \rightarrow 9_{2,7})$	231	
219.764	$HCOOCH_{3(v=1)}$	$(18_{9,9} \rightarrow 17_{9,8})$E	342	1.2					
219.798	$HNCO_{(v=0)}$	$(10_{0,10} \rightarrow 9_{0,9})$	58						
219.822	$HCOOCH_{3(v=1)}$	$(18_{10,9} \rightarrow 17_{10,8})$A	355	1.2	219.822	$HCOOCH_{3(v=1)}$	$(18_{10,8} \rightarrow 17_{10,7})$A	355	1.2
219.827*	$HCOOCH_{3(v=1)}$	$(18_{12,7} \rightarrow 17_{12,6})$E	384	2.3					
219.908	$H_2^{13}CO$	$(3_{1,2} \rightarrow 2_{1,1})$	33	†					
219.949	$SO_{(v=0)}$	$(6_5 \rightarrow 5_4)$	35	†					
220.030	$HCOOCH_{3(v=1)}$	$(18_{9,10} \rightarrow 17_{9,9})$A	342		220.030	$HCOOCH_{3(v=1)}$	$(18_{9,9} \rightarrow 17_{9,8})$A	342	
220.043	$HCOOCH_{3(v=1)}$	$(18_{11,8} \rightarrow 17_{11,7})$E	368	2.3					
220.078	$CH_3OH_{(v_t=0)}$	$(8_{0,8} \rightarrow 7_{1,6})$	97						
220.167	$HCOOCH_{3(v=0)}$	$(17_{4,13} \rightarrow 16_{4,12})$E	103	†					
220.178	CH_2CO	$(11_{1,11} \rightarrow 10_{1,10})$	76	†					
220.190	$HCOOCH_{3(v=0)}$	$(17_{4,13} \rightarrow 16_{4,12})$A	103						
220.258	$HCOOCH_{3(v=1)}$	$(24_{2,23} \rightarrow 24_{1,24})$E	355	1.3					
220.296	$CH_3^{13}CN$	$(12_9 \rightarrow 11_9)$	646	1.3					
220.307	$HCOOCH_{3(v=1)}$	$(18_{10,9} \rightarrow 17_{10,8})$E	354	1.2					
220.368	$HCOOCH_{3(v=1)}$	$(18_{8,11} \rightarrow 17_{8,10})$A	331	2.2	220.370	$HCOOCH_{3(v=1)}$	$(18_{8,10} \rightarrow 17_{8,9})$A	331	2.2
					220.366	$HCOOCH_{3(v=0)}$	$(33_{5,28} \rightarrow 33_{5,29})$E	357	2.2
220.399	^{13}CO	$(2 \rightarrow 1)$	16	†					
220.409	$HCOOCH_{3(v=1)}$	$(18_{4,15} \rightarrow 17_{4,14})$E	299	1.3					
220.476	$CH_3CN_{(v=0)}$	$(12_8 \rightarrow 11_8)$	526						
220.539	$CH_3CN_{(v=0)}$	$(12_7 \rightarrow 11_7)$	419						
220.570	$CH_3^{13}CN$	$(12_4 \rightarrow 11_4)$	183						
220.594	$CH_3CN_{(v=0)}$	$(12_6 \rightarrow 11_6)$	326						
220.621	$CH_3^{13}CN$	$(12_2 \rightarrow 11_2)$	97	†					
220.641	$CH_3CN_{(v=0)}$	$(12_5 \rightarrow 11_5)$	248						
220.647	$HCOOCH_{3(v=1)}$	$(18_{9,10} \rightarrow 17_{9,9})$E	342	2.2					
220.661	$CH_3CH_2CN_{(v=0)}$	$(25_{2,24} \rightarrow 24_{2,23})$	143	2.3					
220.679	$CH_3CN_{(v=0)}$	$(12_4 \rightarrow 11_4)$	183						
220.709	$CH_3CN_{(v=0)}$	$(12_3 \rightarrow 11_3)$	133						
220.730	$CH_3CN_{(v=0)}$	$(12_2 \rightarrow 11_2)$	98	†					
220.743	$CH_3CN_{(v=0)}$	$(12_1 \rightarrow 11_1)$	76						
220.747	$CH_3CN_{(v=0)}$	$(12_0 \rightarrow 11_0)$	69						

Note. *a*. Tentative detections (intensity $\sim 3\sigma$ rms) are marked with "*";
b. Unidentified lines are denoted as "UL", and possible transitions are given;
c. "A(E)A(E)" indicates 4 types of transitions are possible for a certain line: AA, EE, AE, EA;
d. Lines with † are imaged in Figure 3;
Without any digital annotation indicates that the lines are detected in both IRS1 and MM1, especially showing absorption or an (inverse) P-Cygni profile towards IRS1-peak;
"1.1" denote the lines being detected in IRS1 only, especially showing absorption or an (inverse) P-cygni profile towards IRS1-peak.
"1.2" denote the lines being detected in IRS1 only, especially showing pure emission towards IRS1-peak.
"1.3" denote the lines being detected in IRS1-mmS only, but without clear detection in IRS1-peak.
"2.2" denote the lines being detected in both IRS1 and MM1, especially showing pure emission towards IRS1-peak.
"2.3" denote the lines being detected in both IRS1 and MM1, but without clear detection in IRS1-peak.
"3" denote the lines being detected only in MM1.

Table A2: Integrated intensity $\int T_B(\upsilon)d\upsilon$ (Kkm s^{-1}) for NGC 7538S and IRS1-mmS, $\int \tau_(\upsilon)d\upsilon$ (km s^{-1}) for IRS1-peak,corresponding to the transitions shown in Figure A2.

Species	Freq (GHz)	MM1	MM2	MM3	JetN	JetS	IRS1 – mmS	IRS1 – peak
$C^{18}O$	219.56	$120.82_{\pm0.42}$	$24.22_{\pm0.47}$	$5.80_{\pm0.15}$	$20.96_{\pm0.09}$	$27.52_{\pm0.26}$	$\nabla\nabla$	$1.26_{\pm0.02}$
^{13}CO	220.399	$144.74_{\pm6.38}$	$47.60_{\pm0.88}$	≥ 8.13	$36.47_{\pm1.53}$	$55.36_{\pm3.84}$	$\nabla\nabla$	$11.82_{\pm0.18}$
H_2CO	218.476	$43.20_{\pm1.89}$	$51.35_{\pm0.38}$	≤ 1.04	$24.68_{\pm0.55}$	$11.89_{\pm0.59}$	$225.81_{\pm12.56}$	$2.16_{\pm0.00}$
$H_2^{13}CO$	219.909	$9.24_{\pm0.13}$	$24.95_{\pm0.31}$	≤ 0.81	≤ 0.54	$7.87_{\pm0.02}$	$72.24_{\pm1.31}$	$0.07_{\pm0.00}$
CH_2CO	220.178	$5.77_{\pm0.36}$	$22.09_{\pm0.17}$	≤ 0.97	$1.78_{\pm0.06}$	≤ 0.61	$117.79_{\pm1.30}$	≤ 0.03
CH_3OH	218.44	$76.22_{\pm0.69}$	$101.27_{\pm0.89}$	$16.25_{\pm0.13}$	$7.59_{\pm0.72}$	$12.87_{\pm0.35}$	$316.60_{\pm10.35}$	$1.84_{\pm0.03}$
$HCOOCH_3$	220.167	$24.08_{\pm0.36}$	$14.13^{\S}_{\pm0.08}$	≤ 0.78	≤ 0.65	$0.25^{\S}_{\pm0.04}$	$112.05_{\pm20.48}$	≤ 0.06
$?CH_3OCH_3^*$	217.191	$17.80_{\pm0.07}$	$5.10_{\pm0.51}$	≤ 1.14	≤ 0.94	≤ 0.93	$131.87_{\pm1.37}$	$\nabla\nabla$
DCN	217.239	$65.97_{\pm0.18}$	$5.40_{\pm0.65}$	≤ 0.94	≤ 0.83	$5.73_{\pm0.82}$	$98.58_{\pm6.93}$	$0.92_{\pm0.00}$
HNCO	218.981	$43.66_{\pm0.35}$	$26.13_{\pm0.06}$	≤ 0.57	≤ 0.72	≤ 0.39	$83.03_{\pm3.19}$	$0.62_{\pm0.05}$
HC_3N	218.325	$163.85_{\pm0.96}$	$56.58_{\pm0.75}$	≤ 0.92	≤ 0.63	$10.42_{\pm0.53}$	$63.66_{\pm1.58}$	$0.46_{\pm0.01}$
$HC_3N(v_7 = 1)$	218.861	$54.90_{\pm0.56}$	$7.84_{\pm0.27}$	≤ 0.91	≤ 0.63	≤ 1.51	$10.35_{\pm1.24}$	$0.18_{\pm0.01}$
CH_3CN	220.73	$136.57_{\pm1.93}$	$46.87_{\pm1.40}$	$3.97_{\pm0.02}$	≤ 0.38	≤ 1.28	$280.88_{\pm3.92}$	$0.91_{\pm0.03}$
$CH_3^{13}CN$	220.621	$10.43_{\pm1.00}$	$0.60_{\pm0.03}$	≤ 0.29	≤ 0.22	≤ 0.21	$9.03_{\pm0.66}$	≤ 0.04
CH_3CH_2CN	218.39	$21.32_{\pm0.10}$	≤ 0.54	≤ 0.92	≤ 0.63	≤ 1.28	$10.13_{\pm0.79}$	≤ 0.09
NH_2CHO	218.46	$8.30_{\pm0.89}$	$19.77_{\pm0.28}$	≤ 0.54	$0.97_{\pm0.41}$	≤ 0.69	$87.89_{\pm2.66}$	$0.19_{\pm0.01}$
OCS	218.903	$147.54_{\pm0.97}$	$98.99_{\pm0.24}$	$17.04_{\pm0.53}$	$3.49_{\pm0.06}$	$5.28_{\pm0.60}$	$250.85_{\pm3.88}$	≤ 0.14
$O^{13}CS$	218.199	$8.72_{\pm0.66}$	$7.48_{\pm2.62}$	$8.86^{\S}_{\pm0.12}$	≤ 0.83	≤ 1.10	$11.78_{\pm6.42}$	≤ 0.14
SO_2	219.276	$98.07_{\pm0.26}$	≤ 0.67	≤ 0.58	≤ 0.53	≤ 0.88	$30.03_{\pm5.17}$	$0.25_{\pm0.01}$
$^{34}SO_2$	219.355	$102.32_{\pm0.58}$	≤ 0.68	≤ 0.39	≤ 0.47	≤ 1.29	$12.80_{\pm0.18}$	$0.03_{\pm0.00}$
SO	219.949	$223.73_{\pm2.95}$	$123.71_{\pm4.35}$	≤ 1.37	$22.98_{\pm0.51}$	$132.20_{\pm3.98}$	$229.06_{\pm0.66}$	$1.90_{\pm0.06}$
^{33}SO	217.833	$26.83_{\pm0.08}$	$2.97_{\pm0.83}$	≤ 0.33	≤ 0.26	≤ 0.64	$5.23_{\pm1.94}$	≤ 0.11

Note.
1). Most species are measured from Gaussian fits, and uncertainties (written in subscript) on the measured intensities are typically $\leq 10\%$.
2). For those marked with "§", integration has been performed down to the noise level due to their non-Gaussian profile. Uncertainties area however derived from the difference with the Gaussian fit.
3). For species which are not detected, an upper limit derived from 3σ rms is given.
4). "$\nabla\nabla$" indicates no meaningful area can be derived because of obvious absorption in IRS1-mmS, orobvious emission in IRS1-peak.
5). A lower limit is given to species which has partly absorption in NGC 7538 S because of the missing short space.
6). "*" indicates the tentative detected species because only one unblended line has been detected, which has not been observed in our source previously.

Table A3: Laboratory parameters of CH_3CN and HNCO and the intensity integrated over the width of each line $\int T_B(\upsilon)d\upsilon$, which is used for rotation diagrams in Figure 4. Uncertainties on the measured intensities are typically ≤ 10% as determined from Gaussian fit.

Mol.	Freq (GHz)	K	I(300K) Log_{10}	E_L (cm^{-1})	$S_{ul}\mu^2$ (D^2)	o-/p-	MM1 (K km s^{-1})	MM2 (K km s^{-1})	IRS1 – mmS (K km s^{-1})	Note
	220.476	8	-3.098	357.938	205.033	p-	24.76 ± 2.50	5.53 ± 0.09	38.15 ± 0.92	
	220.539	7	-2.868	283.608	243.499	p-	32.99 ± 2.60	13.07 ± 0.16	46.61 ± 4.02	
	220.594	6	-2.377	219.154	553.690	o-	129.85 ± 10.78	60.20 ± 0.08	166.07 ± 2.04	
	220.641	5	-2.522	164.592	305.047	p-	109.82 ± 4.97	36.07 ± 0.18	165.53 ± 11.26	
CH_3CN (J = 12 → 11)	220.679	4	-2.397	119.933	328.188	p-	105.81 ± 3.19	39.42 ± 0.22	225.55 ± 3.57	*1, 2, 3*
	220.709	3	-2.001	85.187	692.234	o-	173.43 ± 7.99	66.98 ± 0.72	287.13 ± 2.31	
	220.730	2	-2.234	60.363	358.988	p-	136.57 ± 1.93	46.87 ± 1.40	280.88 ± 3.92	
	220.743	1	-2.194	45.467	366.614	p-	143.27 ± 31.70	54.19 ± 0.70	301.46 ± 4.56	
	220.747	0	-2.180	40.501	369.277	p-	155.20 ± 31.70	58.70 ± 0.70	326.57 ± 4.56	
	218.981		-2.677	62.949	70.596		35.32 ± 1.11	17.38 ± 0.19	88.86 ± 3.25	
	219.656		-3.232	293.596	59.063		3.41 ± 0.04	3.86 ± 0.03	8.49 ± 0.49	
HNCO	219.737		-2.887	151.337	66.110		25.47 ± 0.12 *	14.07 ± 0.09 *	46.96 ± 0.24 *	*1, 2, 4, 5*
	219.798		-2.602	32.994	72.127		65.23 ± 0.60	36.89 ± 0.18	121.44 ± 6.06	

Notes: *1.* Integrated intensities are obtained by Gildas "Gaussian" fits.
2. Laboratory parameters are from CDMS.
3. Q(300K, CH_3CN)=14683.6324
4. Q(300K, HNCO)=7785.741
5. "*" denotes the line with blending multiplets due to our spectral resolution, and the values are giving by simply taking into account their relative weights.

Table A4: Beam averaged column densities and abundances for O-bearing molecules from different substructures in NGC 7538S and IRS1 denoted in Figure 3.

Species	MM1 (172 ± 23 K)	MM2 (137 ± 14 K)	MM3 (50 K)	JetN (150 K)	JetS (150 K)	IRS1 – mmS (162 ± 14 K)	IRS1 – peak (214 ± 66 K)
I. Column densities (in the form of $x \pm y(z) = (x \pm y) \times 10^z cm^{-2}$)							
$C^{18}O$	$2.71_{\pm 0.31}(17)$	$4.43_{\pm 0.32}(16)$	$4.80_{\pm 0.13}(15)$	$4.16_{\pm 0.02}(16)$	$5.46_{\pm 0.05}(16)$	−−	$7.23_{\pm 5.17}(17)$
^{13}CO †	$4.35_{\pm 0.35}(18)$	$7.79_{\pm 0.56}(17)$	$\geq 6.01(16)$	$5.76_{\pm 0.24}(17)$	$8.74_{\pm 0.61}(17)$	−−	$6.71_{\pm 4.81}(18)$
H_2CO	$6.76_{\pm 0.69}(15)$	$6.34_{\pm 0.58}(15)$	$\leq 6.82(13)$	$3.34_{\pm 0.08}(15)$	$1.61_{\pm 0.08}(15)$	$3.31_{\pm 0.13}(16)$	$9.07_{\pm 7.53}(16)$
$H_2^{13}CO$	$2.50_{\pm 0.39}(14)$	$5.06_{\pm 0.57}(14)$	$\leq 5.56(12)$	$\leq 1.22(13)$	$1.79_{\pm 0.00}(14)$	$1.81_{\pm 0.17}(15)$	$5.30_{\pm 5.34}(14)$
CH_2CO	$4.66_{\pm 0.37}(14)$	$1.43_{\pm 0.12}(15)$	$\leq 3.67(13)$	$1.25_{\pm 0.04}(14)$	$\leq 4.28(13)$	$8.95_{\pm 0.68}(15)$	$\leq 5.96(14)$
CH_3OH	$4.61_{\pm 0.88}(16)$	$4.33_{\pm 0.58}(16)$	$2.25_{\pm 0.02}(15)$	$3.72_{\pm 0.35}(15)$	$6.30_{\pm 0.17}(15)$	$1.74_{\pm 0.18}(17)$	$3.36_{\pm 3.98}(17)$
$HCOOCH_3$	$2.91_{\pm 0.39}(16)$	$1.33_{\pm 0.13}(16)$	$\leq 4.95(14)$	$\leq 6.71(14)$	$2.57_{\pm 0.45}(14)$	$1.27_{\pm 0.09}(17)$	$\leq 1.92(16)$
$?CH_3OCH_3^*$	$7.62_{\pm 0.57}(17)$	$1.97_{\pm 0.19}(17)$	$\leq 1.96(17)$	$\leq 3.71(16)$	$\leq 3.67(16)$	$5.43_{\pm 0.19}(18)$	−−
II. Abundances (in the form of $x \pm y(z) = (x \pm y) \times 10^z$)							
$C^{18}O$	$1.60_{\pm 0.50}(-7)$	$2.60_{\pm 0.58}(-8)$	$9.14_{\pm 0.64}(-10)$	$1.64(-7)$	$1.64(-7)$	−−	$1.64(-7)$
^{13}CO †	$1.33_{\pm 0.41}(-6)$	$2.16_{\pm 0.48}(-7)$	$\geq 7.58(-9)$	$1.36_{\pm 0.01}(-6)$	$1.36_{\pm 0.03}(-6)$	−−	$1.52_{\pm 1.09}(-6)$
H_2CO	$4.00_{\pm 1.18}(-9)$	$3.72_{\pm 0.91}(-9)$	$\leq 1.30(-11)$	$1.32_{\pm 0.03}(-8)$	$4.84_{\pm 0.24}(-9)$	−−	$2.06_{\pm 1.71}(-8)$
$H_2^{13}CO$	$1.48_{\pm 0.53}(-10)$	$2.97_{\pm 0.80}(-10)$	$\leq 1.06(-12)$	$\leq 4.81(-11)$	$5.37_{\pm 0.01}(-10)$	−−	$1.20_{\pm 1.21}(-10)$
CH_2CO	$2.76_{\pm 0.74}(-10)$	$8.36_{\pm 1.99}(-10)$	$\leq 6.98(-12)$	$4.94_{\pm 0.17}(-10)$	$\leq 1.29(-10)$	−−	$\leq 1.35(-10)$
CH_3OH	$2.73_{\pm 1.09}(-8)$	$2.54_{\pm 0.75}(-8)$	$4.29_{\pm 0.22}(-10)$	$1.47_{\pm 0.14}(-8)$	$1.89_{\pm 0.05}(-8)$	−−	$7.63_{\pm 9.03}(-8)$
$HCOOCH_3$	$1.72_{\pm 0.58}(-8)$	$7.77_{\pm 1.96}(-9)$	$\leq 9.43(-11)$	$\leq 2.65(-9)$	$7.71_{\pm 1.35}(-10)$	−−	$\leq 4.35(-9)$
$?CH_3OCH_3^*$	$4.51_{\pm 1.19}(-7)$	$1.15_{\pm 0.29}(-7)$	$\leq 3.74(-8)$	$\leq 1.46(-7)$	$\leq 1.10(-7)$	−−	−−

Note.

1). "*" indicates the tentative detected species because only one unblended line has been detected which has not been observed in our source previously.

2). Abundances with respect to H_2 were computed using N_{H_2} derived from dust continuum for MM1–MM3, and from $C^{18}O$ for the other substructures (assuming $x(C^{18}O) \approx 1.64 \times 10^{-7}$; see Table 1)

3). All species are assumed to have the same temperature as CH_3CN in MM1, MM2, and IRS1-mmS.

4). Values of all species in MM3, the outflow regions (JetN and JetS), and IRS1-peak are derived under assumed temperatures (Section 5.1).

5). Molecular column densities are obtained from the strongest transition of each isotopologue by assuming LTE with the excitation temperatures listed in the table head.

6). Uncertainties for the values derived from one transition (written in subscript) are determined from T_{rot}, partition function $Q(T_{rot})$, and fit to $\int T_B(\upsilon)d\upsilon$ (or $\int \tau_(\upsilon)d\upsilon$ in IRS1-peak).

7). For species which are not detected, an upper limit derived from 3σ rms is given.

8). "−−" indicates that the line area could not be computed because it has obvious absorption in IRS1-mmS, or obvious emission in IRS1-peak, or non-detection of both main and rare isotopologues.

9). A lower limit is given to the species which has partial absorption in S because of the missing short spacing.

10). "†" mark the values which are obtained from likely optically thick lines after we we did the optical depth correction in each substructures except for IRS1-peak.

Table A5: Beam averaged column densities and abundances for N-bearing molecules from different substructures in NGC 7538S and IRS1 denoted in Figure 3.

Species	MM1 (172 ± 23 K)	MM2 (137 ± 14 K)	MM3 (50 K)	JetN (150 K)	JetS (150 K)	IRS1 – mmS (162 ± 14 K)	IRS1 – peak (214 ± 66 K)
I. Column densities (in the form of x ± y(z) = (x ± y) × 10^z cm^{-2})							
DCN	$2.15_{\pm0.26}(14)$	$1.43_{\pm0.03}(13)$	≤ 1.19(12)	≤ 2.38(12)	$1.65_{\pm0.24}(13)$	$3.04_{\pm0.05}(14)$	$7.82_{\pm6.14}(14)$
HNCO	**2.64 ± 1.35(15)**	**1.89 ± 1.01(15)**	≤ 2.44(13)	≤ 4.13(13)	≤ 2.27(13)	**5.73 ± 1.45(15)**	$1.04_{\pm0.96}(16)$
HC_3N	$6.33_{\pm0.12}(14)$	$2.11_{\pm0.03}(14)$	≤ 6.60(12)	≤ 2.39(12)	$3.93_{\pm0.20}(13)$	$2.43_{\pm0.03}(14)$	$3.95_{\pm2.03}(14)$
$HC_3N(v_7 = 1)$	$1.38_{\pm0.42}(15)$	$3.08_{\pm1.08}(14)$	≤ 4.04(15)	≤ 2.03(13)	≤ 4.85(13)	$2.88_{\pm0.96}(14)$	$6.89_{\pm0.69}(14)$
CH_3CN †	**4.58 ± 1.97(16)**	**2.64 ± 0.96(15)**	≤ 1.18(15)	−−	−−	**3.87 ± 1.13(16)**	$4.61_{\pm5.14}(15)$
$CH_3^{13}CN$	$5.58_{\pm0.18}(14)$	$2.67_{\pm0.09}(13)$	≤ 9.85(12)	≤ 1.04(13)	≤ 1.00(13)	$4.58_{\pm0.03}(14)$	≤ 1.87(14)
CH_3CH_2CN	$1.70_{\pm0.13}(15)$	≤ 3.77(13)	≤ 8.43(13)	≤ 4.61(13)	≤ 9.41(13)	$7.77_{\pm0.17}(14)$	≤ 1.76(15)
NH_2CHO	$2.91_{\pm0.13}(14)$	$5.46_{\pm0.50}(14)$	≤ 7.11(12)	$2.96_{\pm1.25}(13)$	≤ 2.11(13)	$2.89_{\pm0.18}(15)$	$1.80_{\pm1.68}(15)$
II. Abundances (in the form of x ± y(z) = (x ± y) × 10^z)							
DCN	$1.27_{\pm0.40}(-10)$	$8.41_{\pm1.40}(-12)$	≤ 2.27(−13)	≤ 9.38(−12)	$4.95_{\pm0.71}(-11)$	−−	$1.77_{\pm1.39}(-10)$
HNCO	**1.57 ± 1.21(−9)**	**1.11 ± 0.83(−9)**	≤ 4.64(−12)	≤ 1.63(−10)	≤ 6.80(−11)	−−	$2.35_{\pm2.17}(-9)$
HC_3N	$3.74_{\pm0.74}(-10)$	$1.24_{\pm0.20}(-10)$	≤ 1.26(−12)	≤ 9.43(−12)	$1.18_{\pm0.06}(-10)$	−−	$8.96_{\pm4.60}(-11)$
$HC_3N(v_7 = 1)$	$8.18_{\pm4.39}(-10)$	$1.81_{\pm0.98}(-10)$	≤ 7.69(−10)	≤ 8.01(−11)	≤ 1.46(−10)	−−	$1.56_{\pm0.16}(-10)$
CH_3CN †	**2.71 ± 1.85(−8)**	**1.55 ± 0.86(−9)**	≤ 2.24(−10)	−−	−−	−−	$1.05_{\pm1.17}(-9)$
$CH_3^{13}CN$	$3.30_{\pm0.71}(-10)$	$1.57_{\pm0.28}(-11)$	≤ 1.88(−12)	≤ 4.09(−11)	≤ 3.02(−11)	−−	≤ 4.24(−11)
CH_3CH_2CN	$1.01_{\pm0.27}(-9)$	≤ 2.21(−11)	≤ 1.61(−11)	≤ 1.82(−10)	≤ 2.83(−10)	−−	≤ 4.00(−10)
NH_2CHO	$1.72_{\pm0.39}(-10)$	$3.20_{\pm0.79}(-10)$	≤ 1.35(−12)	$1.17_{\pm0.49}(-10)$	≤ 6.32(−11)	−−	$4.08_{\pm3.81}(-10)$

Note.

1). "*" indicates the tentative detected species because only one unblended line has been detected which has not been observed in our source previously.

2). Abundances with respect to H_2 were computed using N_{H_2} derived from dust continuum for MM1–MM3, and from $C^{18}O$ for the other substructures (assuming $x(C^{18}O) \approx 1.64 \times 10^{-7}$; see Table 1)

3). Values and uncertainties in bold face are obtained directly from the rotation diagram fits in Figure 4, and all the rest species except for HNCO are assumed to have the same temperature as CH_3CN in MM1, MM2, and IRS1-mmS.

4). Values of all species in MM3, the outflow regions (JetN and JetS), and IRS1-peak are derived under assumed temperatures (Section 5.1).

5). Molecular column densities are obtained from the strongest transition of each isotopologue by assuming LTE with the excitation temperatures listed in the table head.

6). Uncertainties for the values derived from one transition (written in subscript) are determined from T_{rot}, partition function $Q(T_{rot})$, and fit to $\int T_B(\upsilon)d\upsilon$ (or $\int \tau_(\upsilon)d\upsilon$ in IRS1-peak).

7). For species which are not detected, an upper limit derived from 3σ rms is given.

8). "−−" indicates that the line area could not be computed because it has obvious absorption in IRS1-mmS, or obvious emission in IRS1-peak, or non-detection of both main and rare isotopologues.

9). A lower limit is given to the species which has partial absorption in S because of the missing short spacing.

10). "†" mark the values which are obtained from likely optically thick lines after we we did the optical depth correction in each substructures except for IRS1-peak.

Table A6: Beam averaged column densities and abundances for S-bearing molecules from different substructures in NGC 7538S and IRS1 denoted in Figure 3.

Species	MM1 (172 ± 23 K)	MM2 (137 ± 14 K)	MM3 (50 K)	JetN (150 K)	JetS (150 K)	IRS1 – mmS (162 ± 14 K)	IRS1 – peak (214 ± 66 K)
I. Column densities (in the form of $x \pm y(z) = (x \pm y) \times 10^z cm^{-2}$)							
OCS †	$5.86_{\pm 0.26}(16)$	$4.41_{\pm 0.10}(16)$	$6.42_{\pm 0.20}(16)$	≤ 1.10(16)	≤ 6.57(15)	$8.71_{\pm 0.14}(16)$	≤ 2.87(15)
$O^{13}CS$	$7.63_{\pm 0.15}(14)$	$6.05_{\pm 1.92}(14)$	$9.27_{\pm 0.13}(14)$	≤ 6.88(13)	≤ 9.11(13)	$1.01_{\pm 0.50}(15)$	≤ 4.15(15)
SO_2	$1.93_{\pm 0.20}(17)$	≤ 1.57(15)	≤ 2.65(16)	≤ 1.13(15)	≤ 1.89(15)	$6.12_{\pm 1.56}(16)$	$9.71_{\pm 4.18}(16)$
$^{34}SO_2$	$1.38_{\pm 0.20}(16)$	≤ 7.17(13)	≤ 1.95(13)	≤ 5.41(13)	≤ 1.50(14)	$1.62_{\pm 0.13}(15)$	$1.17_{\pm 1.20}(15)$
SO †	$3.16_{\pm 0.31}(17)$	$2.45_{\pm 0.12}(16)$	−−	≤ 1.56(16)	≤ 2.44(16)	$6.91_{\pm 0.47}(16)$	$1.52_{\pm 1.10}(16)$
^{33}SO	$2.81_{\pm 0.30}(15)$	$2.59_{\pm 0.46}(14)$	≤ 1.52(13)	≤ 2.45(13)	≤ 5.96(13)	$5.22_{\pm 1.43}(14)$	≤ 9.85(14)
II. Abundances (in the form of $x \pm y(z) = (x \pm y) \times 10^z$)							
OCS †	$3.47_{\pm 0.79}(-8)$	$2.58_{\pm 0.43}(-8)$	$1.22_{\pm 0.09}(-8)$	≤ 4.33(−8)	≤ 1.97(−8)	−−	≤ 6.52(−10)
$O^{13}CS$	$4.52_{\pm 0.90}(-10)$	$3.55_{\pm 1.79}(-10)$	$1.77_{\pm 0.10}(-10)$	≤ 2.71(−10)	≤ 2.74(−10)	−−	≤ 9.42(−10)
SO_2	$1.14_{\pm 0.34}(-7)$	≤ 9.21(−10)	≤ 5.05(−9)	≤ 4.47(−9)	≤ 5.67(−9)	−−	$2.20_{\pm 0.95}(-8)$
$^{34}SO_2$	$8.19_{\pm 2.80}(-9)$	≤ 4.21(−11)	≤ 3.71(−12)	≤ 2.13(−10)	≤ 4.51(−10)	−−	$2.67_{\pm 2.71}(-10)$
SO †	$2.11_{\pm 0.64}(-7)$	$1.93_{\pm 0.66}(-8)$	−−	≤ 1.23(−8)	≤ 2.27(−8)	−−	$3.45_{\pm 2.49}(-9)$
^{33}SO	$1.66_{\pm 0.50}(-9)$	$1.52_{\pm 0.52}(-10)$	≤ 2.90(−12)	≤ 9.66(−11)	≤ 1.79(−10)	−−	≤ 2.23(−10)

Note.

1). "*" indicates the tentative detected species because only one unblended line has been detected which has not been observed in our source previously.

2). Abundances with respect to H_2 were computed using N_{H_2} derived from dust continuum for MM1–MM3, and from $C^{18}O$ for the other substructures (assuming $x(C^{18}O) \approx 1.64 \times 10^{-7}$; see Table 1)

3). All species are assumed to have the same temperature as CH_3CN in MM1, MM2, and IRS1-mmS.

4). Values of all species in MM3, the outflow regions (JetN and JetS), and IRS1-peak are derived under assumed temperatures (Section 5.1).

5). Molecular column densities are obtained from the strongest transition of each isotopologue by assuming LTE with the excitation temperatures listed in the table head.

6). Uncertainties for the values derived from one transition (written in subscript) are determined from T_{rot}, partition function $Q(T_{rot})$, and fit to $\int T_B(\upsilon)d\upsilon$ (or $\int \tau_(\upsilon)d\upsilon$ in IRS1-peak).

7). For species which are not detected, an upper limit derived from 3σ rms is given.

8). "−−" indicates that the line area could not be computed because it has obvious absorption in IRS1-mmS, or obvious emission in IRS1-peak, or non-detection of both main and rare isotopologues.

9). An lower limit is given to the species which has partial absorption in S because of the missing short spacing.

10). "†" mark the values which are obtained from likely optically thick lines after we we did the optical depth correction in each substructures except for IRS1-peak.

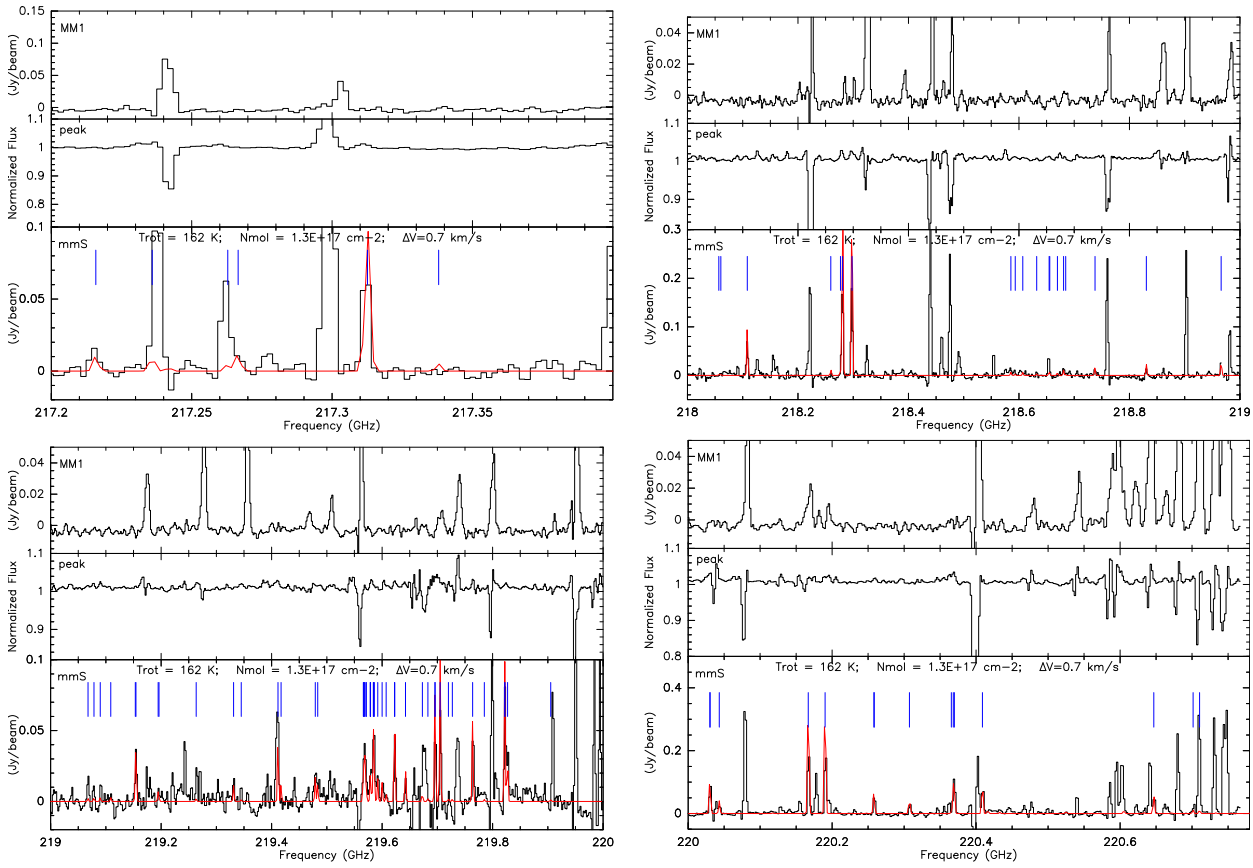

Fig. A1: Synthetic fits of $HCOOCH_3$ in NGC 7538 IRS1 (mmS and peak) and MM1. Black lines represent the observed spectra while red lines show the best-fit model based on optically thin assumption.

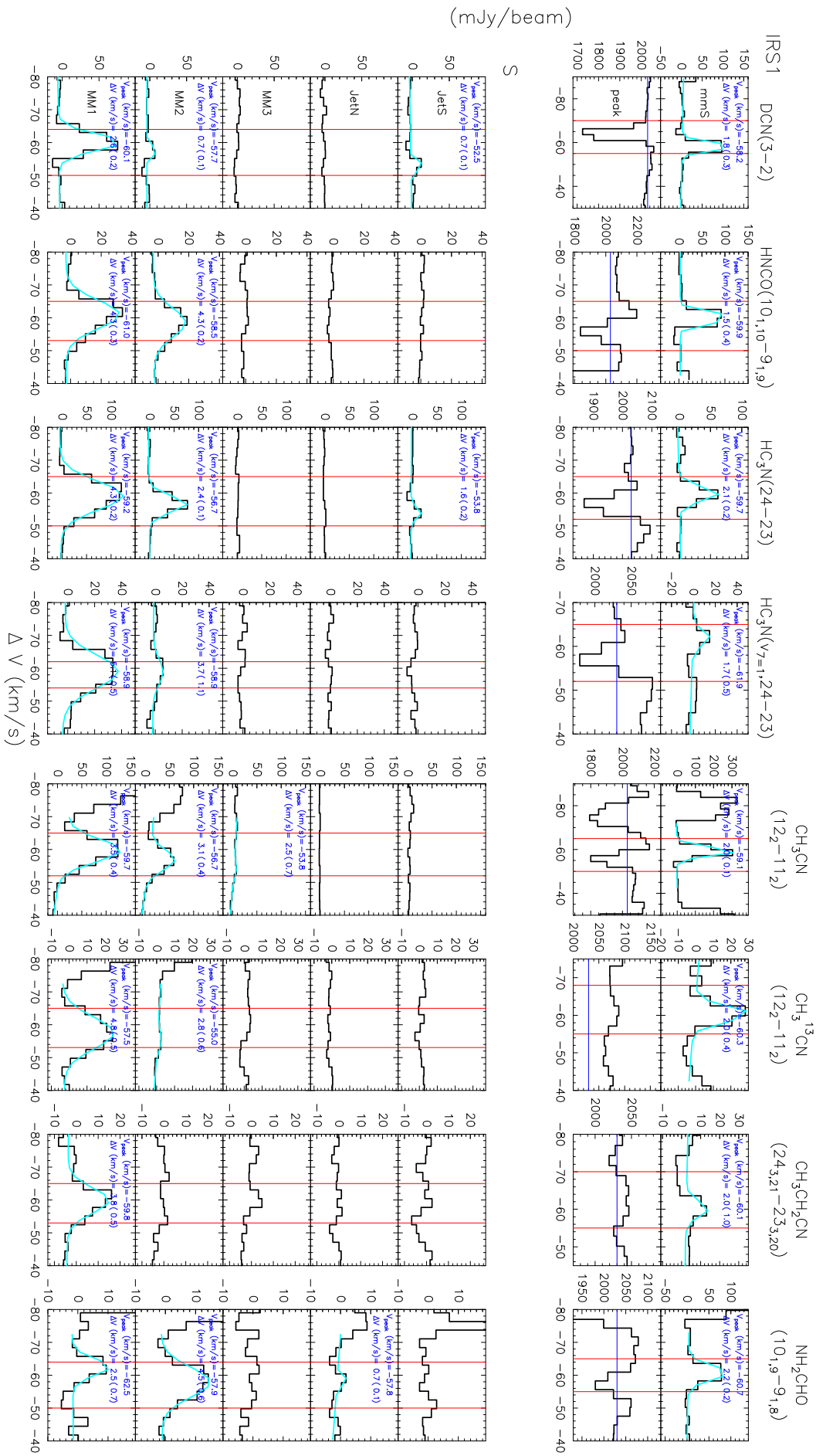

Fig. A2: Line profiles of identified species (in black) and single Gaussian fits (in blue) toward the continuum substructures identified in this paper (given in Table 1). Continuum is not subtracted in IRS1. Two red vertical lines in each panel mark the velocity range we use to integrate the intensity and obtain the spatial distribution maps (Figure 3). Lines marked with "**" has > 4σ detection but could not be fitted with a single Gaussian. "$\nabla\nabla$" denotes the lines having > 4σ detection but showing obvious absorption in IRS1-mmS or obvious emission in IRS1-peak.

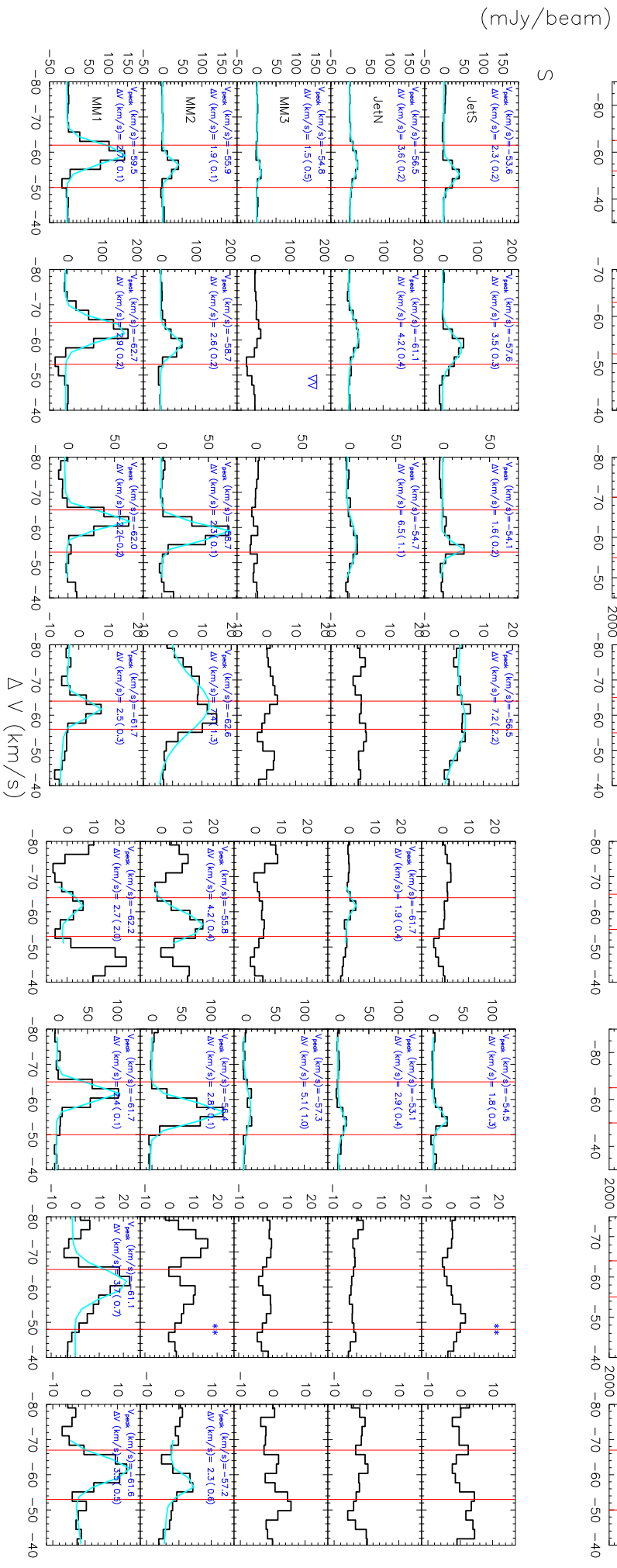

Fig. A2: (continued)

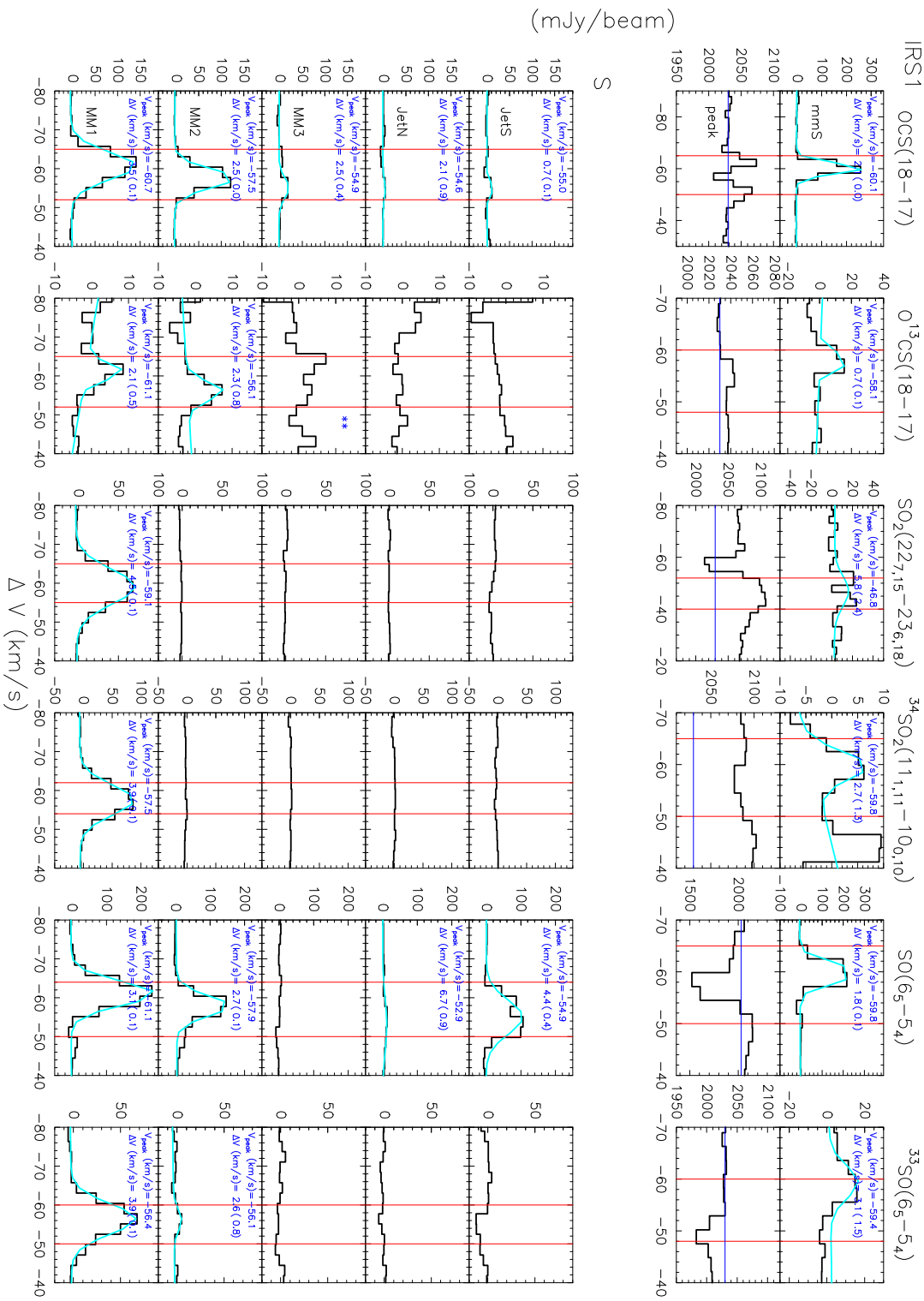

Fig. A2: (continued)